INDIRECT MEASUREMENT OF COSMIC-RAY PROTON SPECTRUM USING EARTH'S γ-RAY DATA FROM *FERMI* LARGE AREA TELESCOPE

PATOMPORN PAYOUNGKHAMDEE

A THESIS SUBMITTED IN PARTIAL FULFILLMENT
OF THE REQUIREMENTS FOR
THE DEGREE OF MASTER OF SCIENCE (PHYSICS)
FACULTY OF GRADUATE STUDIES
MAHIDOL UNIVERSITY
2021

Thesis
entitled

.....
Mr. Patomporn Payoungkhamdee
Candidate

.....
Asst. Prof. Warit Mitthumsiri,
Ph.D. (Physics)
Major advisor

.....
Prof. David Ruffolo,
Ph.D. (Physics)
Co-advisor

.....
Prof. Patcharee Lertrit,
M.D., Ph.D. (Biochemistry)
Dean
Faculty of Graduate Studies
Mahidol University

.....
Assoc. Prof. Kittiwit Matan,
Ph.D. (Physics)
Program Director
Master of Science Program in Physics
(International Program)
Faculty of Science
Mahidol University

Thesis
entitled

was submitted to the Faculty of Graduate Studies, Mahidol University
for the degree of Master of Science (Physics)
on
June 14, 2021

.....
Mr. Patomporn Payoungkhamdee
Candidate

.....
Asst. Prof. Waraporn Nuntiyakul,
Ph.D. (Physics)
Chair

.....
Asst. Prof. Warit Mitthumsiri,
Ph.D. (Physics)
Member

.....
Prof. David Ruffolo,
Ph.D. (Physics)
Member

.....
Prof. Patcharee Lertrit,
M.D., Ph.D. (Biochemistry)
Dean
Faculty of Graduate Studies
Mahidol University

.....
Assoc. Prof. Palangpon Kongsaree,
Ph.D. (Organic Chemistry)
Dean
Faculty of Science
Mahidol University

ACKNOWLEDGEMENTS

Thanks to the members of space physics laboratory.. (will be filled)

Patomporn Payoungkhamdee

INDIRECT MEASUREMENT OF COSMIC-RAY PROTON SPECTRUM USING EARTH'S γ-RAY DATA FROM *FERMI* LARGE AREA TELESCOPE.

PATOMPORN PAYOUNGKHAMDEE 6138171 SCPY/M

M.Sc. (PHYSICS)

THESIS ADVISORY COMMITTEE: WARIT MITTHUMSIRI, Ph.D. (PHYSICS), DAVID RUFFOLO, Ph.D. (PHYSICS)

ABSTRACT

Cosmic rays (CRs) are high-energy particles, mostly protons, propagating in space. The rigidity (momentum per charge) spectrum of CRs is well described by a power law for which the spectral index is approximately 2.8 around 30 - 1000 GV. Recent measurements by PAMELA and AMS-02 indicate an abrupt change of the CR proton spectral index at about 340 GV. When CRs interact with the Earth's upper atmosphere, γ rays can be produced and detected by space-based detectors. Here we use the Earth's γ-ray data collected by the *Fermi* Large Area Telescope along with a proton-air interaction model to indirectly determine the CR proton spectral index and compare against observations by other instruments.

KEY WORDS: COSMIC RAYS / EARTH'S GAMMA RAYS

68 pages

CONTENTS

CONTENTS (cont.)

LIST OF TABLES

LIST OF FIGURES

CHAPTER I
INTRODUCTION

1.1 Overview

Space is full of fascinating phenomena and the questions, from why stars are bright to more advanced questions such as the nature of dark matter. Human curiosity has brought us so far that now we can observe the sky with more sophisticated techniques. However, the research to gather new knowledge by studying the space is endless. The answer to one question sometimes generates another mystery. Research in physical science also helps to create new technology because of the need to overcome challenging limitations of the instruments or techniques.

The frontier of astrophysical research is continually expanding over time because the exploration of one thing does open the new door to another dark room which has been waiting for human to shine a light to explore. There are various branches in astrophysics from theoretical foundation, simulation and experimental physics which all complement of them trying to push the frontier of human knowledge. To study high energy particle accelerators in the universe, the possibility of direct probing of multiple Galactic sources which produce high-energy particles, or cosmic rays (CRs), is nearly impossible in terms of current technology and resources required. Nevertheless, the technology of observing the particles arriving the Earth is more plausible for scientists.

CRs can be observed with two types of detectors: ground-based and spaced-based. Analyzing and studying CR data allows us to interpret the properties of their sources and cosmic environment.

The spectrum of CRs follows a power law with different spectral indices depending on the rigidity (momentum per charge) range of particles. There are multiple types of CR sources in space including unknown sources. Consequently,

changing of the spectral index from one rigidity to another rigidity will find the discontinuity if there is the translation from one source type to another source from the superposition of multiple spectrums.

Fermi-LAT has been launched to orbit around the Earth and monitor the γ-ray sky. Interestingly, the brightest γ-ray source in the sky for the LAT is the Earth's limb due to its proximity. At above 1 GeV, the Earth's γ-ray emission from CRs interacting with the upper atmosphere appears as a bright ring (Abdo et al. 2009).

Before 2010, there were some hints of the abrupt change in the CR spectral index at 300 GV in rigidity by some experiments (Adriani et al. 2011; Seo et al. 2004; Isbert et al. 2002; Haino et al. 2004), though the conclusion was from the combination of data from different experiments which is prone to the systematic uncertainty. In 2014, *Fermi*-LAT attempted to measure this spectral feature indirectly using the Earth's γ-ray emission data from 5 years of observations (Ackermann et al. 2014). The inferred spectral indices are consistent with other experiment, showing a spectral break at around 300 GV with $\approx 1\sigma$ significance level, which is not high enough to make a definitive conclusion.

1.2 Objectives

The objectives of this study are to

- To indirectly measure the CR proton spectrum between approximately 60 – 1000 GV in rigidity.
- To build on the results from the previous study with more dataset
- To improve the optimization technique by using the heuristical methodology
- To reduce the calculation time by inventing a new parallel code in low level from scratch

1.3 Outline of thesis

The dissertation provides various information from the overview introductory context to the technical detail employed in this study as well as the results and interpretations. It is structured as follows.

Chapter I provides the overview and objectives of this work.

Chapter II is the background knowledge relating to this study. This chapter also provides brief history of cosmic ray research which contains impactful experiments and important findings which have advanced the field. Some theoretical detail will be provided along with the historical discoveries. Subchapters describe in more detail about high-energy astroparticle physics.

Chapter III consists of multiple literature reviews involving the study to clarify the theoretical idea as well as for filling the concepts which are important for our better understanding of the next chapter.

Chapter IV consists of datasets selection, flux calculation , computation optimization and interpretation. The following chapter which is chapter V will be the discussion from the analyzed results. The last chapter

The last chapter (Chapter V) is the final summarization from this study. It composed of the final numerical results and the statistical significance.

CHAPTER II
BACKGROUND

2.1 Cosmic ray

This section discusses the historical discoveries from early studies in the field to the latest high-impact experiments.

2.1.1 History

In 1909, Theodor Wolf conducted the famous experiment that pioneered the study of cosmic rays (CRs) by taking an apparatus to measure the rate of ionization from the ground to the top of the Eiffel Tower in Paris (Gray 1949). The result showed that the ionization rate was increased but the magnitude is much lower than the expectation from the underground radioactivity which provided a clue that the origin of CRs was from outer space rather than from the Earth (Hörandel 2013).

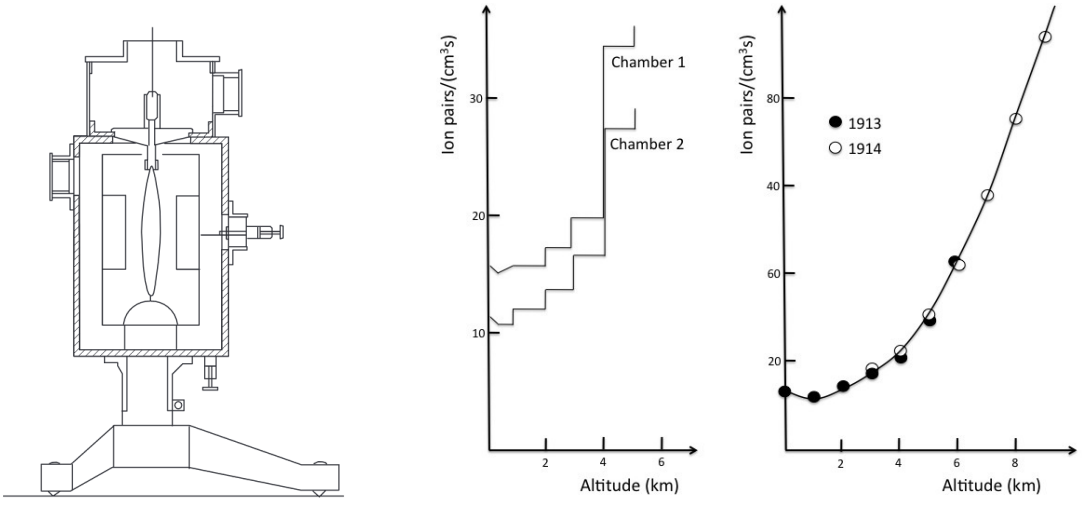

(a) An early version schematic view of electrometer used by Thedor Wulf

(b) Ionization rate from Victor Hess (left) and Werner Kolhörster (right)

Figure 2.1: Wulf's apparatus and the balloon experimental results

However, the experiment measuring the effect of altitude variation with a tiny altitude scale compared to the Earth's atmospheric thickness may not provide enough data. They found that the ionization rate has increased by a quarter compared to that at ground level (De Angelis 2014). Three years later, a risky investigation was conducted by an Australian gentleman who brought a detector and himself to fly with a balloon. His name is Victor Hess, and his name went so famous because he risked his life with the experiment and his flying over 5 kilometers above the ground (Hess 1912). The result is strongly significant and impactful to the astrophysical research community. Risking life In 1914, Werner Kolhörster repeated the balloon experiment with higher altitude up to 9 kilometers from sea level and the ionization rate still increased when the ballon flew higher. These results emphasized that the source of the ionizing ray came from Earth's upper atmosphere or the outer space.

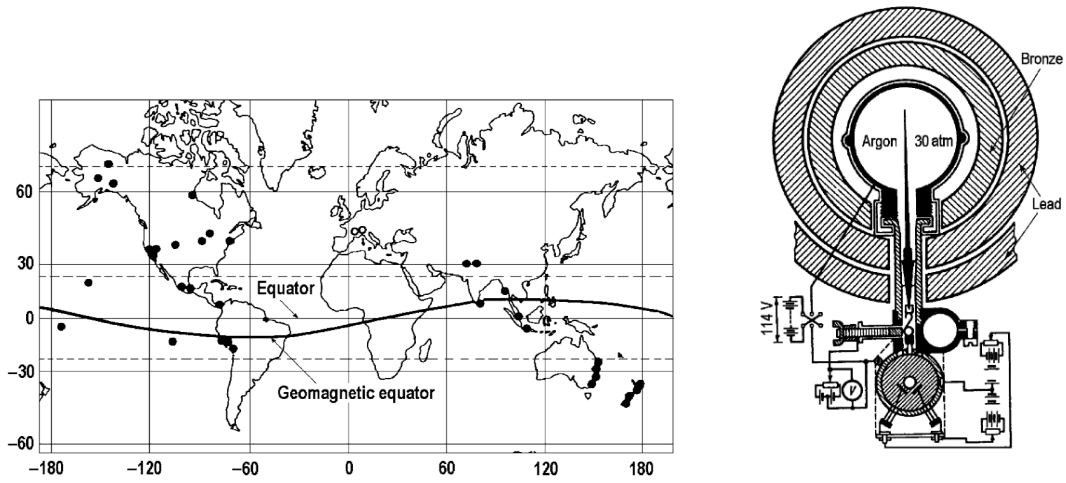

Figure 2.2: (left) Clay's experiment on the geographical variation of CR intensity. Main locations where CR intensity was measured during 8 Compton's expeditions in 1932. (right) The Pb-shielded ionization chamber, organized by Compton. Image is taken from Dorman (2009)

Not only does the ionization rate varies with altitude, the measured rate also depends on the geographical locations. The first experiment was done by John Clay who sailed the ship across the ocean from Holland to Java (Clay 1927, 1928). The geographical locations where CR intensities were measured and the apparatus schematical draft are shown in Figure 2.2. The result shows that

the further from the equator, the higher CR intensity. Another exploration for the geographic variation was done by John Compton in the following five years. He sailed the ship from Sydney (southern hemisphere) to Vancouver (northern hemisphere) for various seasons from 1936 to 1937 back and forth (Compton & Turner 1937). Figure 2.3 demonstrates the latitude variation and the seasonality effects of the multiple trips from the experiment.

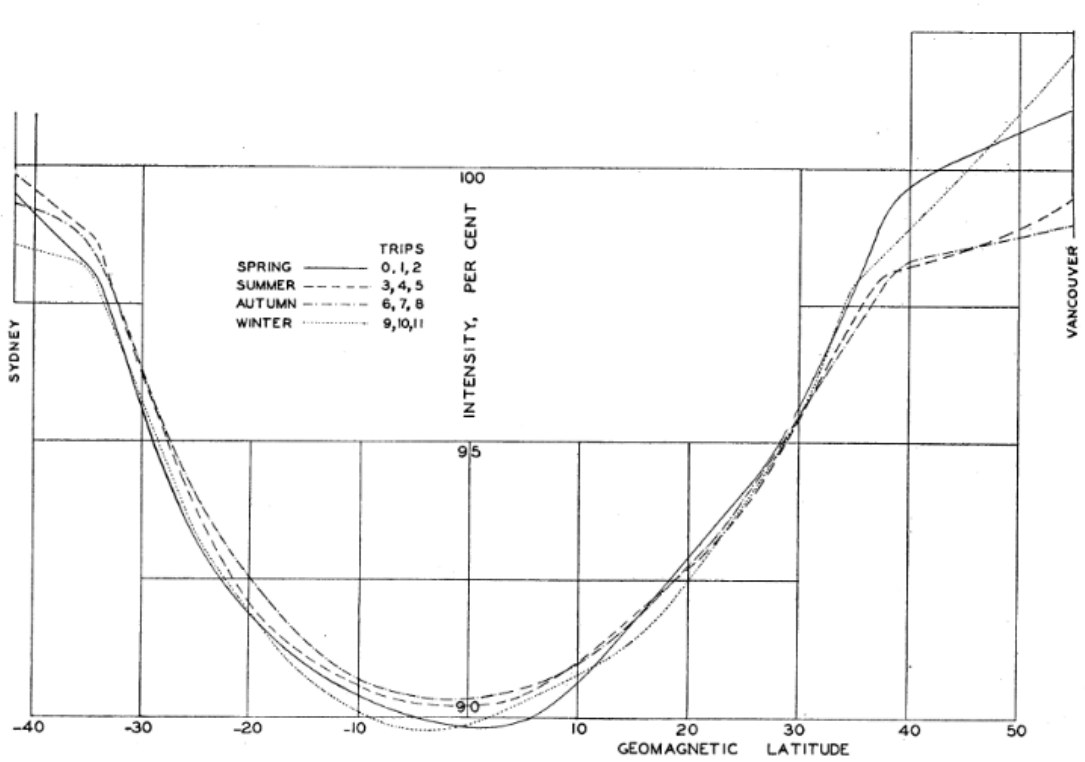

Figure 2.3: Latitude variation of CR intensity for various seasons (Compton & Turner 1937)

The first interpretation study from the discovery has been done by Störmer (1934). The explanation of the CR's altitude variation came from the trajectory of CR particles due to geomagnetic field. In that period, the topic of the geomagnetic field effects on CRs were quite famous. Another impactful study of the CR trajectories under the influence of the Earth's magnetic field was conducted by Bruno Rossi. He studied an assymetry of the East-West distribution of CR flux due to the Lorentz force effects on charged particles by the Earth's magnetic field. He found that the flux is enhanced from the West and interpreted that CRs are predominantly positively charged (Rossi & Greisen 1941).

Ground-based detectors can detect atmospheric particles from CR-air interactions. A space-based detector can also inspect the East-West asymmetry effect from a low Earth orbit. In 2008, *Fermi*-LAT was launched to observe γ rays, and also electrons, and has clearly observed the East-West effect in the spectrum at a few GeV (Madlee et al. 2020).

2.1.2 Physical properties

CRs are high-energy particles propagating through space. CRs gain their momentum from various acceleration mechanisms CRs gain their momentum such as supernovae, created by astrophysical objects. The composition of CRs consists of approximately 90% protons, 8% alphas, and other nuclei of heavier elements (Dembinski et al. 2017). Experimentally, many observations indicate that the CR spectra for all particles and individually do follow the power law in rigidity (momentum per charge) for which the spectral index depends on the energy range. Theoretically, the observed spectrum in a broad energy range is the superposition of CRs produced by various types of sources which could exhibit different spectral indices depending on their physical properties.

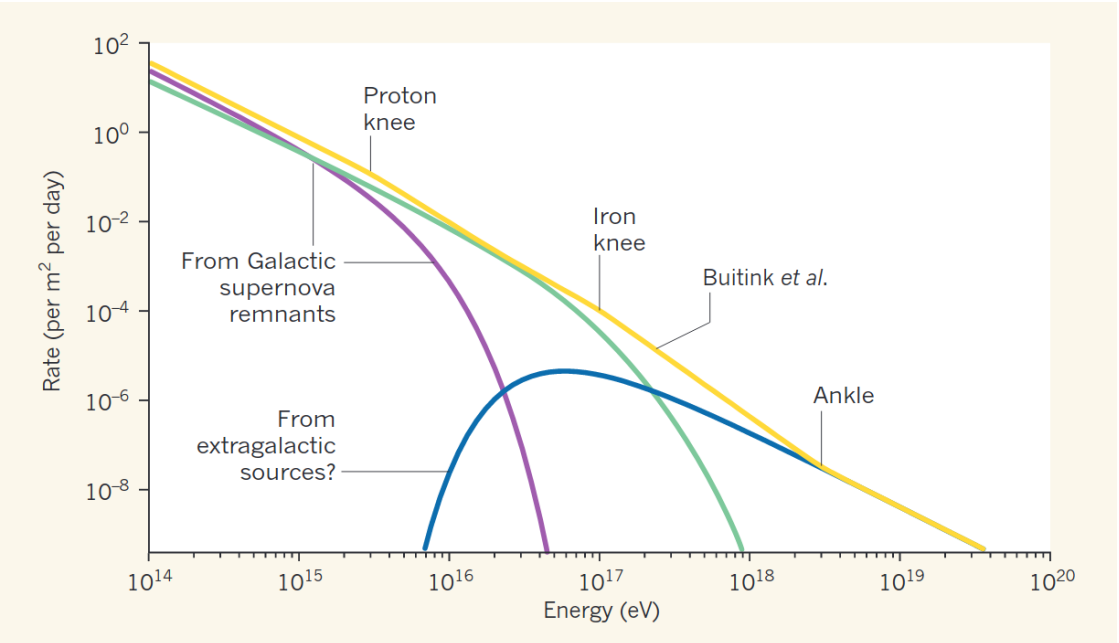

Figure 2.4: The CR spectrum showing the superposition of different populations of sources (Taylor 2016)

Figure 2.4 shows the widely accepted scenario of how each population of CR sources dominates the value of the spectral index for different energy ranges. Three well-established spectral breaking points are the first knee at $\sim 10^{15}$ eV, the second knee at $\sim 10^{17}$ eV, and the ankle at $\sim 10^{19}$ eV. The rate to find one particle with the energy above the first knee is around one particle per square meter per year and the possibility that an apparatus could detect a particle at energy above the ankle is roughly one particle per kilometer per year.

Interestingly, the maximum energy of UHECRs ever detected never exceed ∼2 orders of magnitude above the ankle energy. This upper energy limit of CRs is widely known as the Greisen–Zatsepin–Kuzmin (GZK limit). According to the GZK theory, UHECRs cannot have an energy above a certain limit because UHECRs are produced from distant extragalactic sources and propagate through vast space full of low-energy background photons, the cosmic microwave background. According to the GZK theory, UHECRs cannot have an energy above a certain limit because UHECRs are produced from distant extragalactic sources and propagate through vast space full of low-energy background photons, the cosmic microwave background. When the energy of the UHECRs is above a certain threshold, they would interact with the background photons and lose their energies (Greisen 1966).

CRs can be categorized into two types based on how they are produced:

1. **Primary cosmic rays**: are produced from astrophysical objects which may be within the Solar system, within the Milky Way Galaxy (Galactic CRs), or from extragalactic sources (extragalactic CRs). Some example origins of primary CRs are stellar winds, supernovae, pulsars, active galactic nuclei, and speculative sources such as dark matter decay.

2. **Secondary cosmic rays**: are produced from primary CRs interacting with the Earth's atmosphere. The interactions create showers of hadronic, leptonic, and electromagnetic particles. Researchers have developed and improved Monte Carlo simulations of the CR air showers based on particle physics theory. These models are very useful for secondary CRs studies.

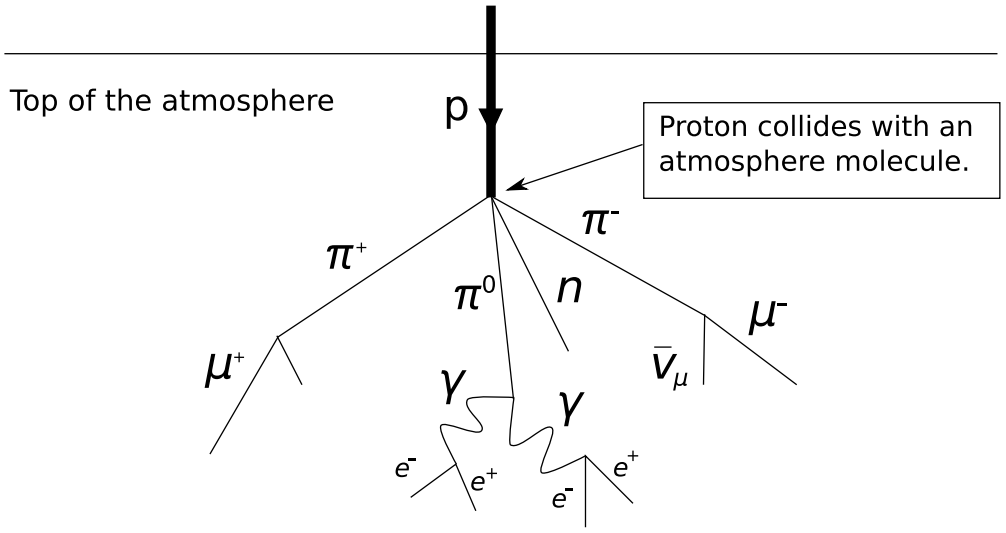

Figure 2.5: Simplified schematic of CR proton air shower (Image taken from Cosmic Rays, Wikipedia, Magnus Manske, 2011)

2.1.3 γ-ray production

The production mechanisms of γ rays are fundamentally different from those for charged particles that can be accelerated with the electromagnetic force. While charged particles can gain or lose energy during their propagation through space, high-energy γ-ray photons tend to only lose energy. Here we briefly discuss the production processes of γ rays.

- **Decaying of unstable matter**: Radioactive decay is one of the most well-known phenomena for the γ-decay mode. One example of heavy-ion decay is cobalt-60. It decays into an excited state of nickel as

  $$^{60}_{27}\mathrm{Co} \longrightarrow {}^{60}_{28}\mathrm{Ni}^{*} + \mathrm{e}^{-} + \bar{\nu} + \gamma\,,$$

  then the excited nickel emits another γ ray to become the stable state

  $$^{60}_{28}\mathrm{Ni}^{*} \longrightarrow {}^{60}_{28}\mathrm{Ni} + \gamma\,.$$

  Some particles, such as the neutral pion (π^0), decay into γ rays. The Feynman's diagram of a π^0 decay is demonstrated in Figure 2.6. The lifetime of π^0 is short, $\sim 8.5 \times 10^{-17}$ seconds. There are some other decay channels (with $< 1\%$ branching ratio) that result in combinations of a photon and pairs of lightweight leptons, as long as the momentum, energy, and quantum

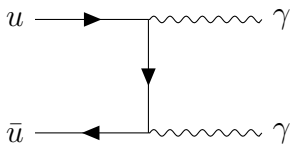

Figure 2.6: Feynman's diagram of the neutral pion (π^0) decay into two γ-rays.

numbers are conserved. Another interesting property of the $\pi^0 \to 2\gamma$ mode is the momentum vectors of the γ-ray pair have the same magnitude but opposite direction in the rest frame of π^0.

- **electron–positron annihilation**: Electron (e^-) and positron (e^+) are the lightest leptons which can annihilate into 2 γ-rays. Heavier and shorter-lived leptons, muon (μ) and tau (τ), can also create γ rays in a similar manner as illustrated in Figure 2.7.

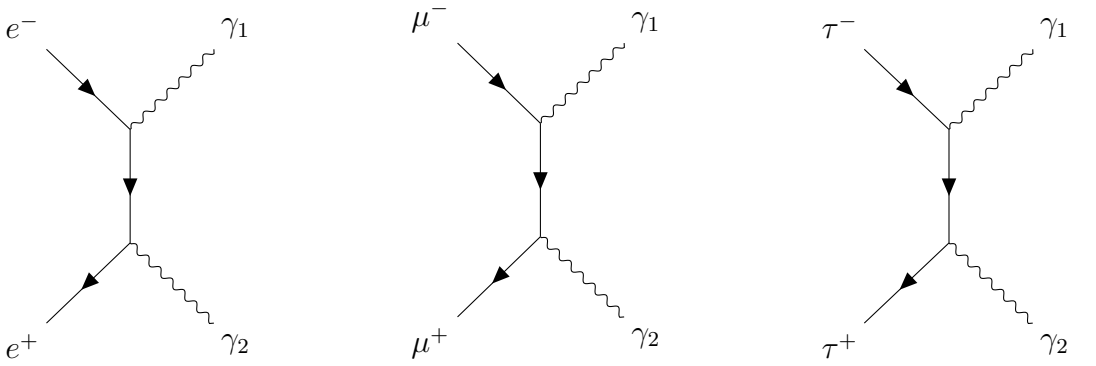

(a) Lightweight leptons (b) Mediumweight leptons (c) Heavyweight leptons

Figure 2.7: Lepton-antilepton annihilation path diagram.

- **Synchrotron & Bremsstrahlung radiation**: It is theoretically and experimentally well known that when charged particles are accelerated, they emit photons. If the acceleration is due to a magnetic field, the emission is called the synchrotron radiation. Humans have built donut-shaped apparatuses inside which charged particles are traveling in a circle guided by strong magnetic fields and produce synchrotron radiation for various applications.

  Another closely related mechanism is the Bremsstrahlung process. When charged particles, typically electrons, move close to heavier positively charged

nuclei, the Coulomb force between them cause an acceleration on the electrons, resulting in Bremsstrahlung radiation.

- **Inverse Compton scattering**

  scattering: A photon can electromagnetically interact with an electron (or any charged particles). The Compton scattering describes a photon losing its energy to an electron. In the opposite situation, a highly relativistic electron can interact and transfer its energy to a low-energy photon to become a γ-ray photon. This process is called the "Inverse Compton scattering" as shown in Feynman's diagram in Figure 2.8.

(a) First branch (b) Second branch

Figure 2.8: First-order Feynman's diagrams for the Compton and Inverse Compton processes.

Astrophysical sources of γ rays

- **Supernova remnants (SNRs) and molecular clouds**: The supernova is a violent explosion of a dead star, causing the material to expand in a spherical shell that sweeps the interstellar medium and decelerates over time. The shock wave from the explosion is believed to produce the shock acceleration of CRs. Three major γ-ray production processes from the SNRs involve hadronic (mostly π^0 decay) cascades, electron bremsstrahlung, and Inverse Compton scattering (Dermer & Powale 2013).

- **Diffused γ-ray emission from the galactic plane**: The plane of the Milky Way galaxy has a high density of gas, dust, stars, and other types of objects. Thus, CRs can interact with such material and create diffuse

emission of γ rays, which is brighter along the Galactic plane as illustrated in Figure 2.9.

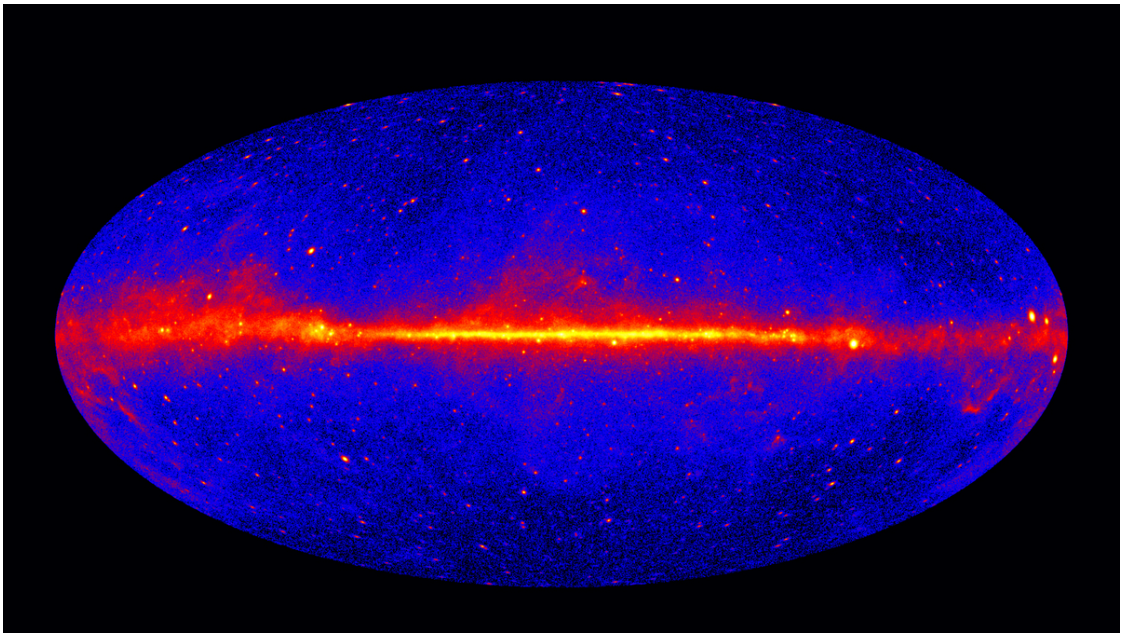

Figure 2.9: Intensity of γ-ray $>$ 1 GeV in galactic coordinates (Image credit: NASA/DOE/*Fermi* LAT Collaboration).

- **Pulsars**: Pulsars are rapidly spinning neutron stars as a result of the supernova explosion of massive stars. They have very strong magnetic fields and can emit bright radiation in a beam from their magnetic poles. The pulsars' intensity could appear to be a periodic emission to observers on Earth due to the pulsars' rotation. They are likely the majority of point sources in the Galactic plane region detected by *Fermi* LAT.

- **Active Galactic Nuclei (AGNs)**: AGN is the center of the active galaxy. The luminosity is much higher than the stars. It produces multi-wavelengths photon in a different band such as radio, microwave, γ-ray and etc. Then this object could be observed from various instruments.

- **Earth's limb γ-ray production**: The closest γ-ray source to the LAT is our Earth's atmosphere. The Earth's upper atmosphere is extremely bright in γ-ray band. The Earth shines in high energy (>100 MeV) γ ray due to the collisions of CRs with the Earth's upper atmosphere producing secondary

particles which include π^0's that quickly decay into γ rays. The Earth's γ-ray emission is the main target source for this study.

2.2 *Fermi* Large Area Telescope (LAT)

One of the famous space telescopes that observes the sky in γ-ray wavelength is the *Fermi* Large Area Telescope (LAT). Formerly, it was called Gamma-ray Large Area Space Telescope (GLAST). The LAT is designed to collect high-energy ($\sim$100 MeV to above 300 GeV) photons data, but it is also able to measure electrons. The orbiting radius is around 550 kilometers from sea level. *Fermi* also carries the Gamma-ray Burst Monitor (GBM) to study γ-ray bursts for seeking exotic events. The telescope was launched on 11 June 2008 and is still currently taking data in 2021.

2.2.1 Overview

Figure 2.10 shows components of *Fermi*. There are two instruments onboard: the Large Area Telescope (LAT) and the Gamma-ray Burst Monitor (GBM). The LAT is the primary instrument that detects γ rays between $\sim$100 MeV to above 300 GeV. The GBM monitors the sky at a lower energy range of $\sim$8 keV to 40 MeV. The GBM consists of two sub-components which are sodium iodide detector for low-energy photons (8 keV to 1 MeV) and bismuth germanate detector for high-energy photons (0.2 MeV to 40 MeV). The GBM monitors transient events and immediately triggers the LAT to point to the locations of the flares for a certain period of time before returning to the normal survey mode.

2.2.2 Large Area Telescope (LAT)

Figure 2.11 illustrates main components of the LAT which are described as follows.

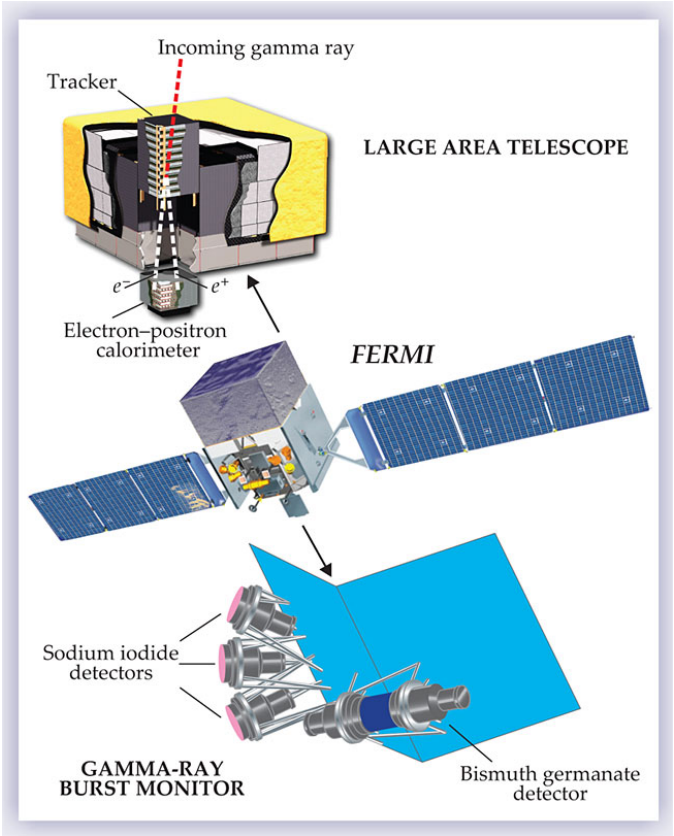

Figure 2.10: Main components of the LAT and the GBM on the *Fermi* Space Telescope (Michelson et al. 2010)

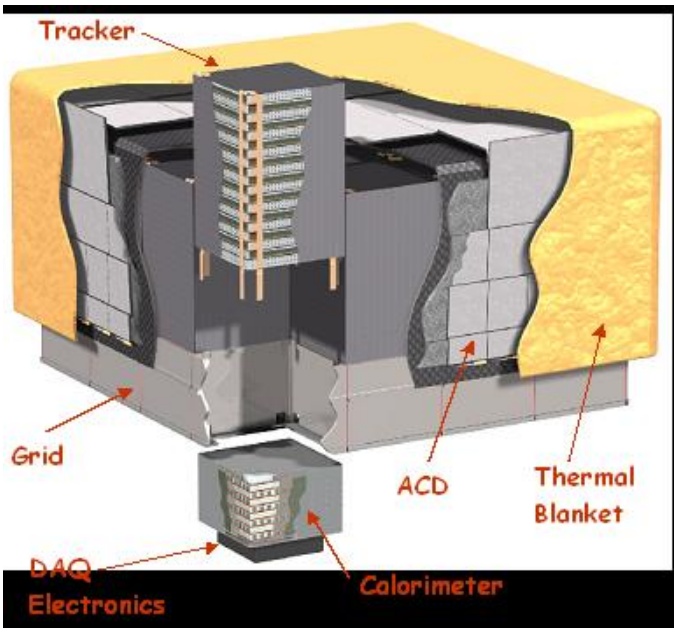

Figure 2.11: Main components of the LAT (Image taken from https://fermi.gsfc.nasa.gov)

Anti-coincidence Detector (ACD)

The ACD consists of 89 plastic scintillator tiles covering four sides and the top of the LAT. Each tile contains two photomultipliers and wavelength shifting fibers embedded in the scintillator. The edges of neighboring tiles are overlapping to reduce the effect of the gaps. The main objective of the ACD is to reject background charged particles which create electrical signals when passing through the scintillator tiles. The estimated efficiency for charged particle identification by the ACD is about 0.9997.

Tracker (TKR)

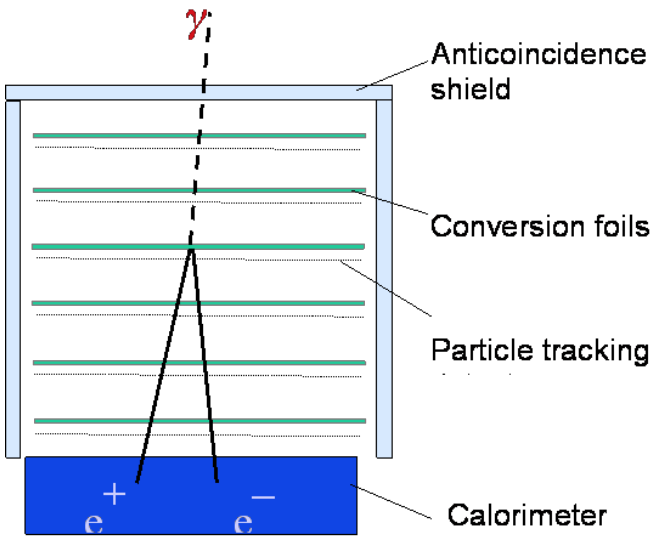

Figure 2.12: Schematic of γ-ray detection of the LAT (Image taken from https://fermi.gsfc.nasa.gov)

The TKR system consists of 16 planes of particle tracking detectors made from silicon strips which are interleaved with tungsten conversion foils as shown in Figure 2.12. An incident γ ray has high probability to interact with the conversion foil and is converted into an e^+e^- pair.

As the e^+e^- pair travel through the silicon strip trackers, they leave their traces on the position sensing detectors, allowing us to reconstruct the direction of the original photon. The narrow gaps between layers of silicon trackers improve the angular resolution of the LAT compared to previous instruments. In Figure 2.13,

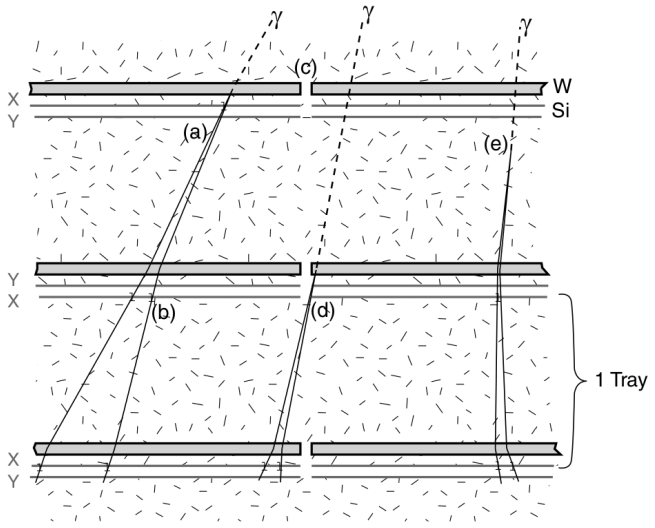

Figure 2.13: LAT's particle tracker. (a) The ideal case where the conversion happens in an early layer and leaves a footprint along with multiple layers (b). (c) The photon skips the first layer and be converted in another layer with a missed hit in 1st and 2nd of Si trackers (d). (e) Conversion occurs in structural materials and is traced by the following Si trackers. (Atwood et al. 2009)

case (a) is the typical situation in which photon is pair-produced by the conversion layer and clean e^+e^- footprints are recorded. Nevertheless, there are some cases, such as (d) in which the e^+e- paths pass through the gap between towers or (e) in which the photon is pair-converted outside of the conversion foil. Having multiple layers of trackers helps the reconstruction of these special cases.

Calorimeter (CAL)

When the e^+e^- pair enters the CAL, they radiate their energy in the CsI crystal scintillators, producing electronic readout which is proportional to the energy loss of e^+e^- inside the CAL. According to the radiation lengths of e^+ and e^-, the CAL is optimized to contain the e^+e^- showers with energy from 0.1 to a few hundred GeV. Thus, TeV photons could have large uncertainties in their energy reconstruction by the LAT.

The overview apparatus structure is illustrated in Figure 2.14. Each calorimeter module consists of 96 CsI(Tl) scintillator crystals with the size of 2.7 cm x 2.0 cm x 32.6 cm and PIN photodiodes at both ends which connect to the readout electronic components translating the amount of light sparkled in the crystal to

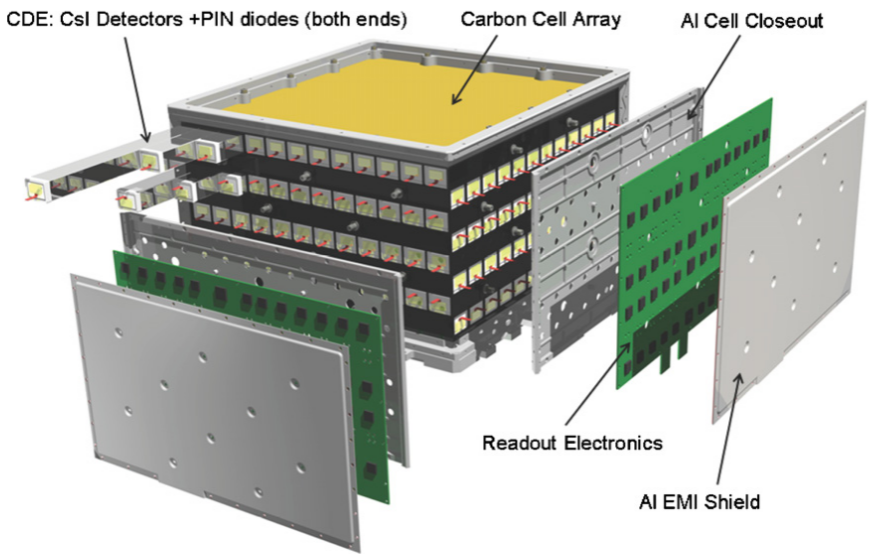

Figure 2.14: LAT's calorimeter (Atwood et al. 2009)

digitized signals. Each horizontal layer is combined from 12 crystal components and stack 8 times by rotating them 90°each for boosting the angular resolution for the sparking lights. A carbon cell was build for supporting the structure of low mass particle tracker due to the properties of high stiffness, thermal conductivity and thermal stability. An electron, position, or γ-ray will deposit the energy in the calorimeter as the scintillated lights via electromagnetic interactions. The segmented crystal allow LAT to trace the showers of particles for spatial imaging.

Data Acquisition System (DAQ)

The DAQ system is designed to reduce the amount of raw data transmitted to the ground through the limited bandwidth.

The lowest-level components are tower electronic modules (TEMs) to serve as the interface for the the TKR and CAL. All TEMs create event buffering and communicate with the Event Builder Module (EBM) which is a component of Global-trigger/ACD-module/Signal Distribution Unit (GASU). Command Response Unit (CRU) is built to communicate the software execution in the DAQ system. Lastly, the Event Processing Unit (EPU) processes a selected event from TEM and ACD Electronics Module (AEM). Filtering an event could reduce the data transmission rate from a few kHz to around 400 Hz to the ground level.

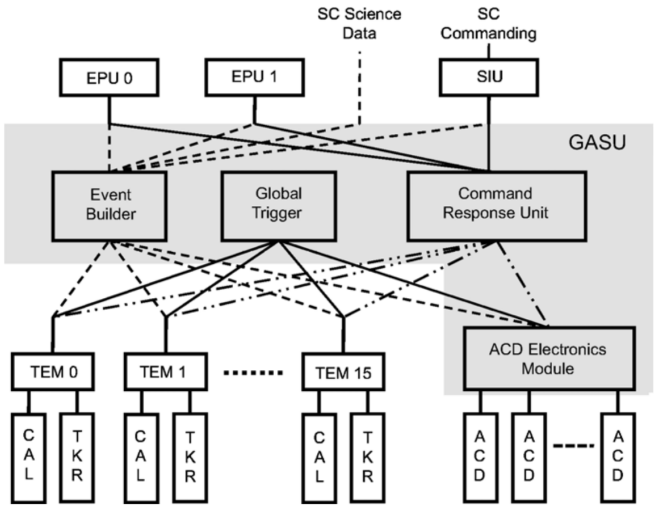

Figure 2.15: Flow chart of LAT's data acquisition system (DAQ) (Image taken from Atwood et al. (2009))

2.2.3 Event reconstruction

Before launch, the event reconstruction algorithm for photons was based entirely on the Monte Carlo (MC) simulations by modeling the photon and background signals in the ACD, TKR, and CAL systems in realistic in-orbit environment. The data processed by this pre-launch event reconstruction algorithm is called "Pass 6" version.

The raw onboard data are called "level 0". After transmitted to the ground and processed, the data become "level 1". After a few years after launch, the LAT collaboration has improved the event reconstruction algorithm and released the "Pass 7" version based on the actual in-flight data. The newest version and likely to be the final version is Pass 8. In each version, photons are organized into different classes (e.g., TRANSIENT, SOURCE, ULTRACLEAN, ULTRACLEANVETO) based on the level of background contamination. The TRANSIENT class has the loosest selection which allows us to obtain better statistics for the observations of faint transient sources but with a trade-off for the highest probability of background contamination. The SOURCE class is optimized for typical source analyses of the LAT, while the ULTRACLEANVETO is the cleanest class with low background contamination but also with the lowest statistics.

2.2.4 LAT performance and characteristics

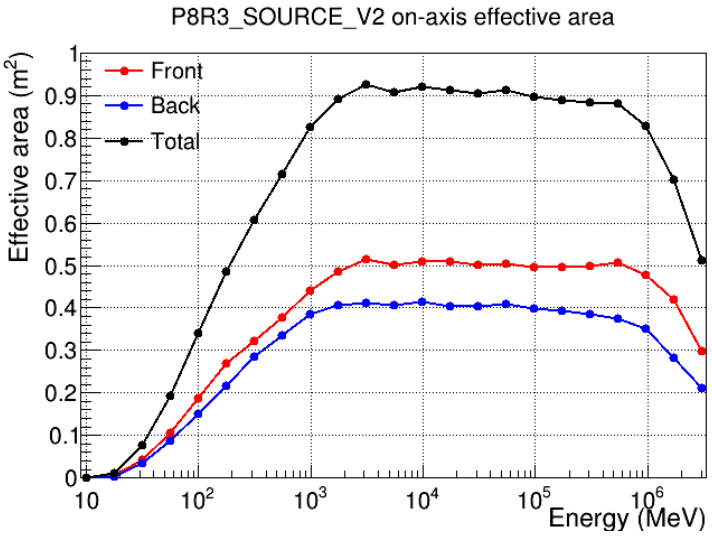

Figure 2.16: LAT's effective area as a function of energy for normally incidence photons (Maldera 2019). Front means the effective area of an event that photon hits the conversion layer at the top and decays into a pair of electron-position. Back represents the effective area of the event that photons pass through the top part and be converted to the bottom of the TKR module. The total effective area (black) is the combination of front and back.

Fermi LAT's physical cross-section area is 1.8 x 1.8 m^2. However, its effective area for particle detection varies as a function of energy and incidence angle. Figure 2.16 shows the LAT's Pass 8 SOURCE effective area for photons arriving perpendicular to the cross section of the LAT as a function of energy, indicating low detection efficiency below ∼100 MeV and above ∼1 TeV. The effective area from front part is higher than the back due to the conversion event that happens in the front leaves more footprint in silicon strip of TKR more than the back.

Another crucial variable relating to the LAT effectiveness is the incidence angle ($\theta_{\rm LAT}$). An event with small $\theta_{\rm LAT}$ would pass through many tracking layers, yielding better detection efficiency. Figure 2.17 shows the relation between the effective area and $\theta_{\rm LAT}$.

Since the structure of the LAT is cube-like, the effective area, therefore, depends on the azimuthal angle ($\phi_{\rm LAT}$) of the photon. Figure 2.17 illustrates the asymmetry of the LAT's effective area as a function of $\phi_{\rm LAT}$, showing four peaks corresponding to corners of the LAT.

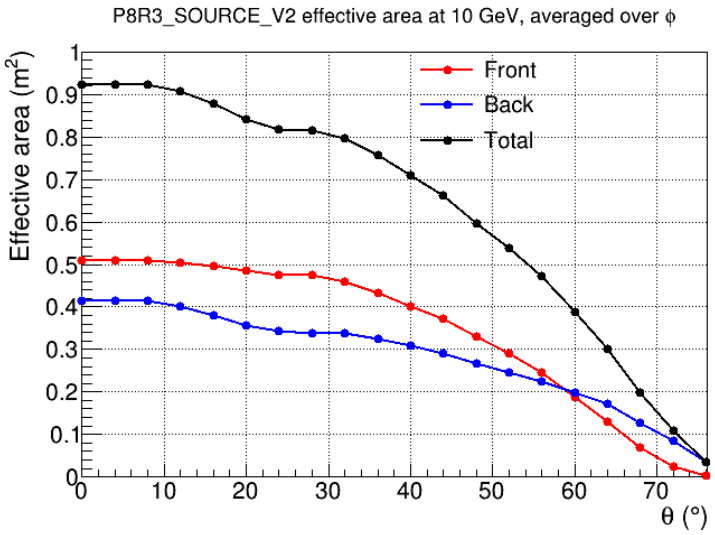

Figure 2.17: Effective area versus incidence angle (Maldera 2019)

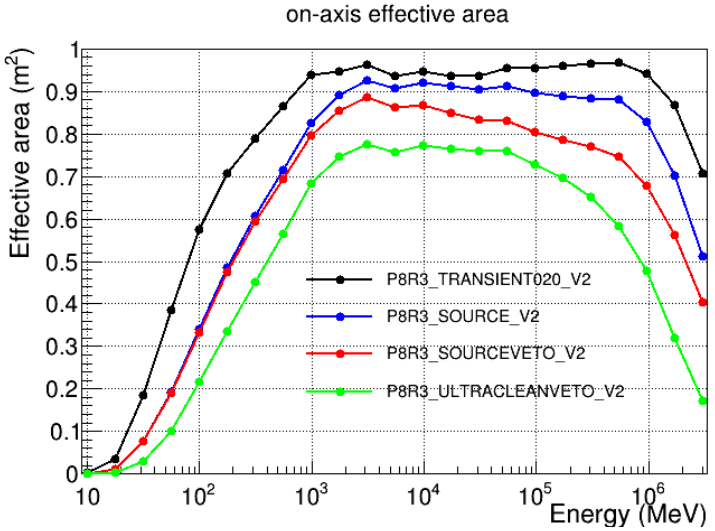

Figure 2.18: Effective area along with the energy of each event class (Maldera 2019)

The event class also has a crucial role when considering the effectiveness of the reconstructed event. The cleanest class namely "ULTRACLEANVETO" would have the smallest effective area. On the other hand, the TRANSIENT class would yield the largest effective area as illustrated in Figure 2.18.

CHAPTER III
LITERATURE REVIEW

Cosmic-ray could come from different origins from galactic sources to extra-galactic sources. ~~The kinetic energy of cosmic rays also highly depends on where does it from.~~ Low energy CRs usually came from the Sun called "solar energetic particle". The production process of solar particle event mostly came from the coronal mass ejection (CME) when high atomic number and energy (HZE) ions were dragged by a magnetic field in the plasma. The extra-galactic CRs typically has high momentum from the extreme condition of the acceleration mechanism in pulsar, quasars and supernova remnant (SNR). The theoretical description of acceleration in SNR and solar flares is the shock wave acceleration in the following paragraph.

One of the most impactful studies of CR's acceleration mechanism was conducted by Fermi (1949). The study describes how high-energy CR particles gain such a huge momentum from the shock wave that was generated by supernovae or a great explosion from the heavy dense star. How it gains the kinetic energy could be described as a first-order shock acceleration and the overall spectrum of charged particles could be represented as the power law ~~in Equation 3.1.~~

$$\frac{dN(E)}{dE} \propto E^{-\gamma} \tag{3.1}$$

where $\gamma \geq 2$ ~~in the non-relativistic regime~~. However, moving magnetized plasma cloud can accelerate the charged particle in the space called "second-order Fermi acceleration". Both regimes were computed the Lorentzian forces regardless of thermal collision in the process.

~~The~~ CR protons are major components in the arrival of CR particles under multiple observations. However, α-particle is also a second important CR particle when considering a precise calculation of CR interactions. The other

majority of heavy weight nuclei that could propagate through space are C, O, Ne and so on. The differential flux in kinetic energy of multiple observations is visualized in Figure 3.1 under the work of Beringer et al. (2012) to take various atomic numbers from various experiments.

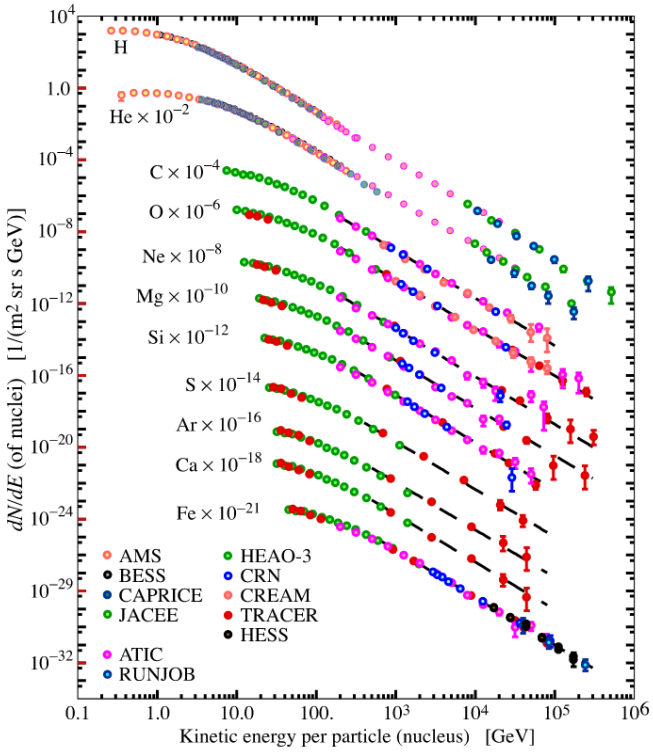

Figure 3.1: Cosmic-ray elemental spectra from various experiments (Beringer et al. 2012)

Since there is a moving plasma inside the Earth, the magnetic field has been generated from the dynamics of the moving charged ions in the plasma. ~~The magnetic field of the Earth has a north pole at the geometric south pole of the Earth and vice versa~~. The Earth's magnetic field plays an important role in the arrival of CR particles because the Lorentzian forces will bend the direction of a moving charged particle depends on the rigidity of the particle. ~~This means the magnetic field line mantles the Earth with a certain direction towards the geometric north pole.~~

Firstly, it creates the CR cutoff rigidity on the terrestrial where each location of the Earth requires a minimum rigidity of incident charged particles as a condition for arrival. Figure 3.2 shows a cutoff rigidity on the Earth's surface.

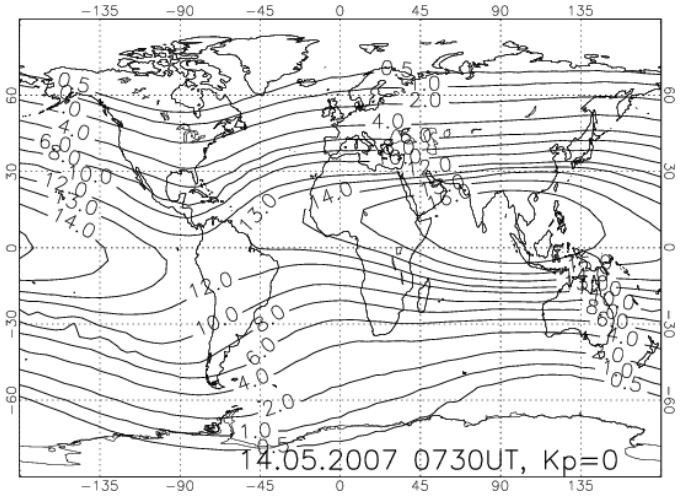

Figure 3.2: World map with computed geomagnetic vertical cutoff rigidity contour lines on a given date (B., Ütikofer, E.O., & LÜCKIGER 2007)

Secondly, incoming charged CRs with a charge have been dragged by the Earth's magnetic. Then a charged particle would move as a curve or a spiral depends on the rigidity of an incoming particle which leads to the East-West effects when an orbiting detector could find more particle on the Westside more than on the East side for a significant level of intensity. A pioneer of Earth's γ-ray experiment is conducted by Kraushaar et al. (1965) where the detector was deployed on the Explorer XI satellite and orbiting in the sky.

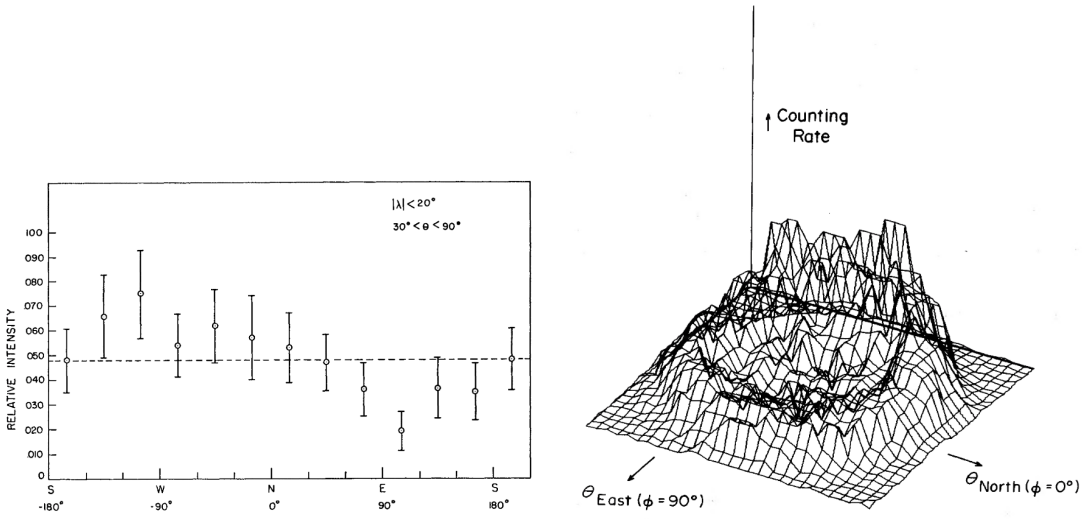

(a) Explorer XI (Kraushaar et al. 1965) (b) OSO-3 (Kraushaar et al. 1972)

Figure 3.3: The asymmetry of γ-rays East-West intensity

The incoming photon from the East and West direction is the crucial evidence of the bending of CRs trajectory by Earth's magnetosphere. The first analysis shows a distinguishable intensity from East to West as visualized in Figure 3.3a. The second experiment where the γ-ray detector is attached to Third Orbiting Solar Observatory (OSO-3) and collecting the γ-ray in MeV range. The 2-D plot of the intensity is shown in Figure 3.3b.

Moreover, An early analysis found that the observing γ-rays intensity along the zenith angle from different geomagnetic latitudes (λ) is differentiable as shown in Figure 3.4. The reason behind this outcome came from the Earth's rigidity where the incoming particles near the equatorial have less chance to arrive than the north pole and likely to interact with the atmospheric molecules and emits the γ-rays. This is the secondary evidence of how geomagnetic fields play an important role on the trajectory of the CR particles.

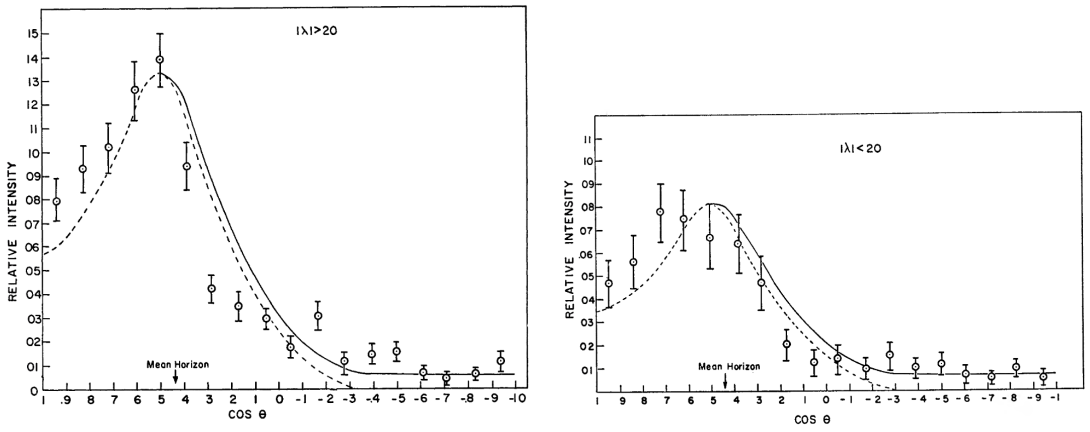

(a) observing above 20°geomagnetic latitude (b) observing below 20°geomagnetic latitude

Figure 3.4: γ-ray intensity along the zenith angle (Kraushaar et al. 1965)

The following experiment of Earth's albedo observations is conducted by sending a second small astronomy satellite (SAS-2) with a higher resolution in angle and observing above 35 MeV up to GeV range (Thompson et al. 1981). The projected 3-D representation of intensity is shown in Figure 3.5a. A few decades later, another precise $\gamma - ray$ detector has been attached to the CGRO satellite (Petry 2005). An outcome from the analysis illustrated the bright region around the Earth's limb region as in Figure 3.5b.

~~The previous details are full of so much experimental evidence. However,~~

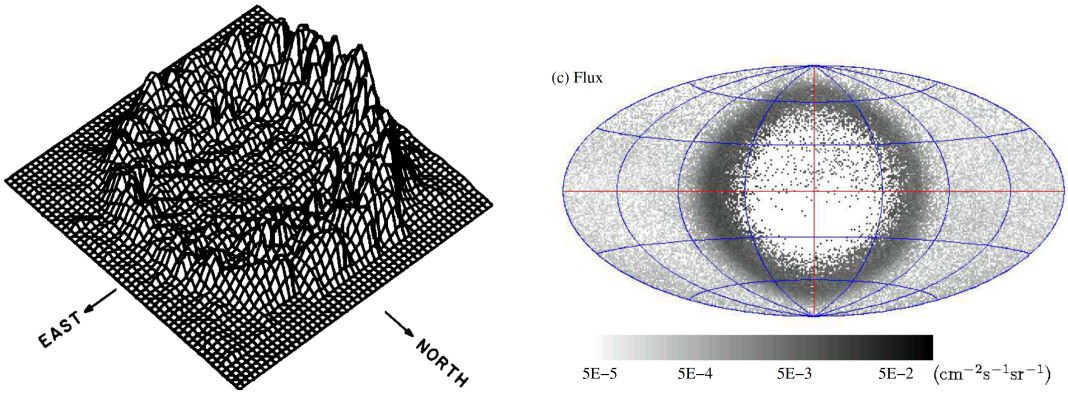

(a) SAS-2 experiment (Thompson et al. 1981) (b) EGRET experiment (Petry 2005)

Figure 3.5: The Earth's centered intensity plot from the satellite based observations

Morris (1984) ~~put the weights on the assumption of the bright region as seen as albedo in γ-ray came from the interaction of proton and the atmospheric nuclei. The study~~ shows the γ-rays intensity and the variation of air depth by differing the zenith angle along limb region as plotted in Figure 3.6 and Thompson et al. (1981) data has been exploited in the analysis.

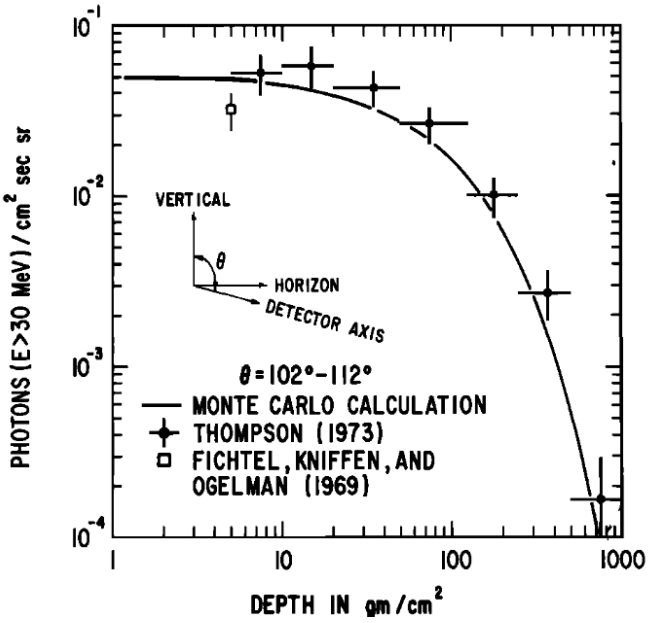

Figure 3.6: Calculated γ-ray intensity with the variation of zenithal angle (Morris 1984)

Furthermore, this study computes the γ-ray spectrum from the bright region as seen as albedo from the Earth's limb and lunar albedo. ~~The~~ Figure

3.7 shows the spectrum from the theoretical calculation. Figure 3.7a identify the 2 bounds of the limb's region with an approximated air depth. Appealingly, another evidence of the solar activity could cause lower arrival CR particles since the propagating magnetic field drag a charged particle towards outer space. The distinguishable spectrum from this phenomenon is demonstrated in Figure 3.7b.

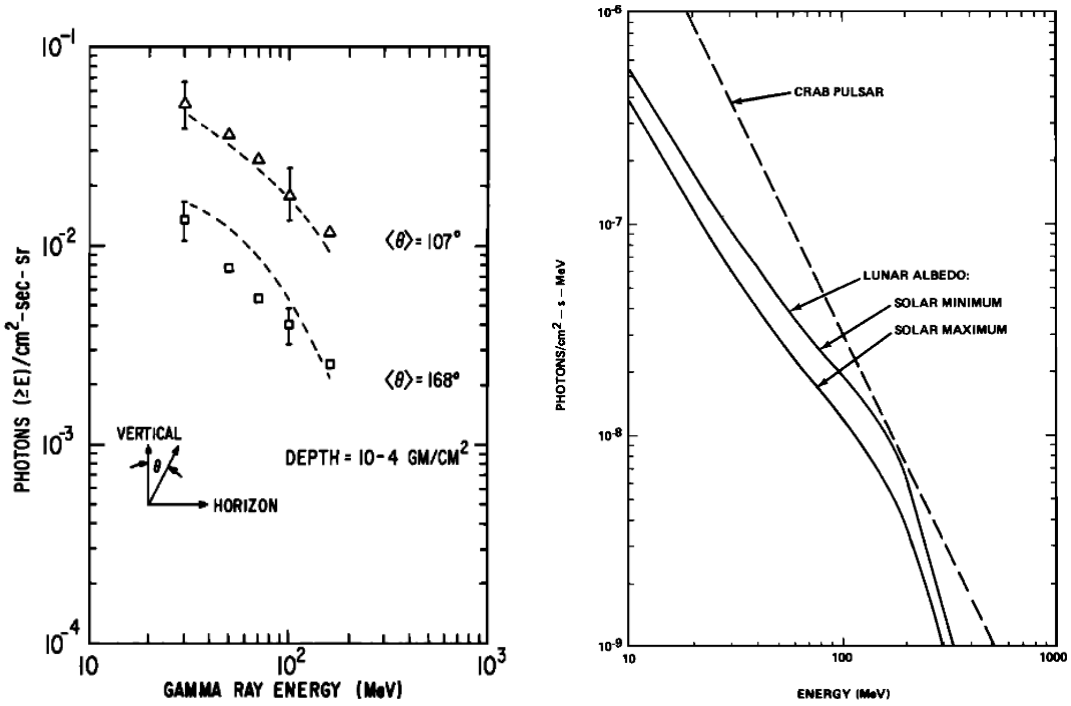

(a) Earth's limb γ-ray spectrum (b) Lunar's atmospheric γ-ray spectrum

Figure 3.7: γ-ray spectrum from proton-nuclei interactions (Morris 1984)

~~Not so long after *Fermi*-LAT was launched in the sky.~~ In 2009, an early examination of the induced γ-ray emission was observed by the most precise γ-ray detector Abdo et al. (2009). Since there is a huge improvement in the technological side which makes LAT capable of detecting high energy γ-ray from MeV up to TeV. Another discovery from this study was the East-West effect ~~is~~ highly depends on the energy ~~where it was converted from the incident energy of CR particles~~. The higher energy means the higher rigidity and it would reflect how hard the magnetic field could bend the trajectory. ~~The intensity was divided into 4 energy ranges from a few GeV to a higher GeV that could be considered as the relativistic scheme where the kinetic energy is much higher than the mass as shown in Figure 3.8.~~

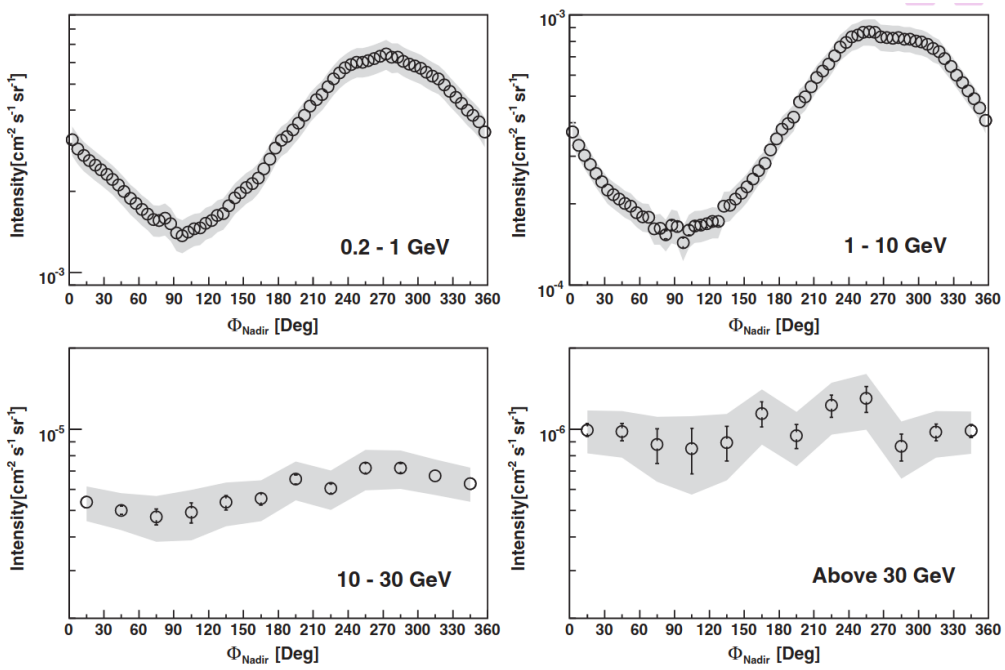

Figure 3.8: γ-rays intensity from limb emission in 4 energy ranges (Abdo et al. 2009)

The objective of this work is to indirectly measure the proton spectrum in GeV range. The direct measurement in an early study of high-energy CR particles such as proton and helium was observed by Haino et al. (2004). Another following experiment is Adriani et al. (2011). ~~Both of them still lack the capability to detect such high energy on a scale of a hundred GeV. Nevertheless, there is a clue about the breaking energy in the proton spectrum with very low statistics and leaves room for further study.~~

Since there is just a clue from the previous direct observations. The indirect measurement of CR proton spectrum has been performed in energy between 90 GeV to 6 TeV by taking advantage of the brightness of Earth's limb from the collision of incident CR protons (Ackermann et al. 2014). The 5 years of γ-ray data have been exploited by investigating the incident proton spectrum via proton-proton collision model for finding whether CR protons have a breaking point of slope in the power law spectrum. The study found that there is a breaking spectral index in the proton spectrum above 200 GeV Nonetheless, Statistical analysis turns out that it is 1σ significant level.

Back in 2011, one of the most efficient space-based CR detectors was launched by the carriage of the Endeavor space shuttle. The detector has been attached to the international space station (ISS). The main mission of AMS-02 is to search antimatter, dark matter from measuring CRs. It can detect antimatter such as position and antiproton. This detector is also able to detect other heavyweight nuclei like B, CNO, Ne, etc. In 2015, a proton spectrum has been directly reported and found the breaking at 340 GV (Aguilar et al. 2015) with very high statistics (confidence level 99.9%). The result from AMS-02 shows the consistency with ~~the~~ other direct measurement from balloon-based and space-based experiments where the spectrum from various observations is plotted in Figure 3.9. In addition, the helium spectrum was also measured and reported in Aguilar et al. (2015).

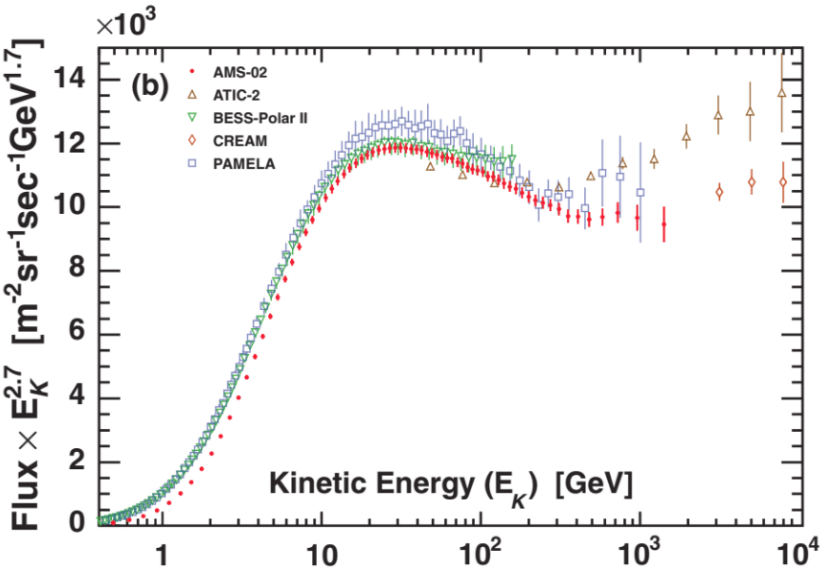

Figure 3.9: CR proton spectrum from AMS-02 and earlier direct measurements (Aguilar et al. 2015)

According to the previous study (Ackermann et al. 2014), low statistical significant potentially came from lack of the dataset or the methodology from the consequence of indirect measurement. In this work, a similar study will be performed with a larger data size from ∼ 9 years of observation. ~~Hopefully, the study could answer the first mentioned clue and put the weights on previous work.~~ Moreover, an improvement of the optimization process by employing the heuristic optimization as well as the high performance calculation of the exposure map for ~~a~~

lesser computational time in γ-ray spectrum calculation.

CHAPTER IV
METHODOLOGY

This chapter gives information on γ-ray flux calculation by providing the information on data filtering and the extracting processes. The recent hadronic interaction model yielding γ rays is discussed. This model is used to reconstruct the CR proton spectrum from the measured γ-ray spectrum. Lastly, the last sub-chapter contains details of statistical analysis.

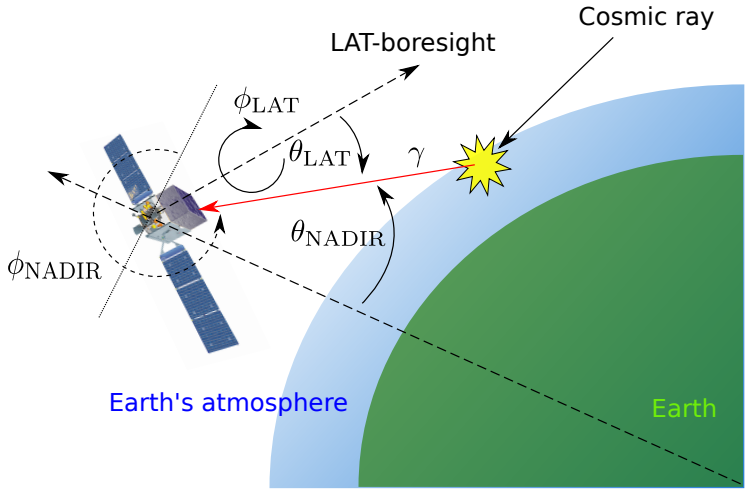

Figure 4.1: Schematics of the Earth's γ-ray production from CR interaction with the upper atmosphere.

Figure 4.1 demonstrates the definitions of some important angular variables describing a photon's direction in this analysis. The nadir angle ($\theta_{\rm NADIR}$) is the angle between a photon's and the nadir direction. The incidence angle ($\theta_{\rm LAT}$) is the angle of a photon's direction with respect to the detector's boresight. The angle $\phi_{\rm LAT}$ specifies the azimuthal angle of a photon in the LAT's reference frame.

4.1 Data selection

In this work, 9 years of LAT's photon and spacecraft data have been used. We use the latest version of event reconstruction (Pass 8) with the cleanest photon event class[1] (ULTRACLEANVETO) in this work. All data sets can be downloaded pubically from the LAT's database website[2].

To select the Earth's limb photon produced in the thin-target regime where the absorption effect could be neglected, we follow the same criteria ($68.4^\circ < \theta_{\rm NADIR} < 70.0^\circ$) used in the previous LAT analysis by Ackermann et al. (2014). We select photons between 10 GeV and 1 TeV which would be correspond to the CR proton rigidity range of roughly 60 GV to 2 TV (Ackermann et al. 2014). We also cut photons with $\theta_{\rm LAT} > 70^\circ$ to avoid mis-reconstructions of highly off-axis photons.

4.2 Flux extraction

The definition of the Earth's limb flux in the energy bin i is given by

$$\textbf{Flux}(E_i) = \frac{dN}{dE}(E_i) = \left(\sum_{\rm pixel} \frac{\rm Count_i}{\rm Exposure_i} \right) \frac{1}{\Delta\Omega\Delta E} \tag{4.1}$$

where $\rm Count_i$ is the photon count ~~map~~, $\rm Exposure_i$ is the exposure ~~map~~, $\Delta\Omega$ is the solid angle size of the limb region, and ΔE is the energy bin width. Since the CR spectrum follows a power law in the energy range of this analysis, we expect a power law in the Earth's γ-ray emission spectrum. Therefore, to calculate the Earth's γ-ray spectrum, we divide the energy into 50 bins equally spaced in log scale from 10 GeV to 1.0 TeV.

The flux calculation procedure can be summarized in the following steps.

1. Analyze 50 bins in energy with equal logarithmic spacing between 10 GeV - 1 TeV

[1] https://fermi.gsfc.nasa.gov/ssc/data/analysis/documentation/Cicerone/Cicerone_Data/LAT_DP.html

[2] https://fermi.gsfc.nasa.gov/ssc/data/access/lat

2. Create 2D histogram count maps from photon data for each energy bin

3. Create 2D histogram exposure maps (effective area × livetime) from spacecraft data for each energy bin

4. Calculate the Earth's γ-ray flux using the count and exposure maps by Equation 4.1

5. Perform background subtraction from an average background distribution (Define background in range $72.0^\circ < \theta_{\mathrm{NADIR}} < 80.0^\circ$)

4.2.1 Exposure map calculation

The exposure map calculation is the most complicated step in this work because we have to perform coordinate transformation. In the standard spacecraft data files, the LAT positions and orientations are recorded in equatorial coordinates. We have to make a coordinate transformation to obtain the position of any given pixel in an exposure map in the spacecraft's reference frame in order to derive the corresponding effective area for that pixel.

Coordinate transformations

Spacecraft's position and orientation (direction of the LAT's boresight and solar panel) are recorded in the equatorial coordinates for which we denote with a symbol "eq". We can define the Cartesian axes for the equatorial coordinate by letting the x-axis ($\hat{x}_{\mathrm{eq}}$) point to the vernal equinox for which the right ascension (RA) is 0° and letting the z-axis point to the pole for which the declination (DEC) is 90°.

We analyze the Earth's γ-ray emission in the local-zenith coordinate system denoted by the symbol "zn," as viewed locally by the LAT. Here we define that $\hat{x}_{\mathrm{zn}}$ points along the local zenith direction of the LAT, and that $\hat{z}_{\mathrm{zn}}$ points perpendicular to $\hat{x}_{\mathrm{zn}}$ in the $\hat{x}_{\mathrm{zn}}$-$\hat{z}_{\mathrm{eq}}$ plane. The "eq" and "zn" coordinate systems are illustrated in Figure 4.2. Here we assume that $\hat{x}_{\mathrm{zn}}$ makes an angle δ_{zn} with the

$\hat{x}_{\rm eq}$ and $\hat{y}_{\rm eq}$ plane, and $\alpha_{\rm zn}$ is the azimuthal angle of $\hat{x}_{\rm zn}$ projection onto the $\hat{x}_{\rm eq}$ and $\hat{y}_{\rm eq}$ plane.

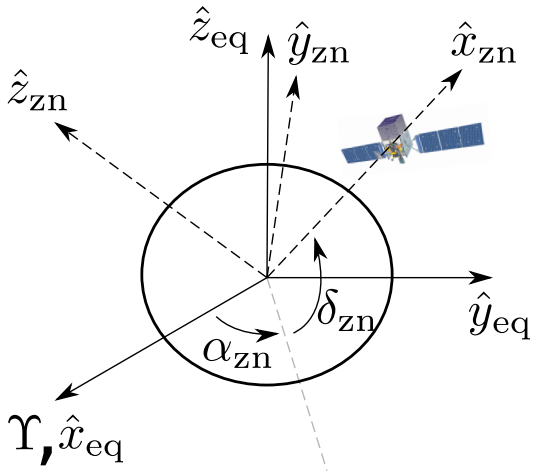

Figure 4.2: Illustration of the relationship between the equatorial (eq) and local-zenith (zn) coordinate systems for the LAT.

We can write the components of the zn system in terms of the eq system as

$$\begin{aligned}
\hat{x}_{\rm zn} &= \cos\delta_{\rm zn}\cos\alpha_{\rm zn}\hat{x}_{\rm eq} + \cos\delta_{\rm zn}\sin\alpha_{\rm zn}\hat{y}_{\rm eq} + \sin\delta_{\rm zn}\hat{z}_{\rm eq} \\
\hat{z}_{\rm zn} &= -\sin\delta_{\rm zn}\cos\alpha_{\rm zn}\hat{x}_{\rm eq} - \sin\delta_{\rm zn}\sin\alpha_{\rm zn}\hat{y}_{\rm eq} + \cos\delta_{\rm zn}\hat{z}_{\rm eq} \\
\hat{y}_{\rm zn} &= \hat{z}_{\rm zn} \times \hat{x}_{\rm zn}.
\end{aligned} \tag{4.2}$$

Equation 4.2 can be written more compactly in a matrix form with

$$\hat{r}_{\rm zn} \equiv T_{\rm eq\to zn}(\delta_{\rm zn}, \alpha_{\rm zn})\hat{r}_{\rm eq}, \tag{4.3}$$

where $T_{\rm eq\to zn}$ is the transformation matrix which depends on the values of $\delta_{\rm zn}$ and $\alpha_{\rm zn}$.

Two variables for determining the LAT boresight orientation are described in equatorial coordinates as declination angle ($\delta_{\rm p}$) and the right ascension angle ($\alpha_{\rm p}$). A full representation of the zn and sp coordinates could be written as Equation 4.4. The compact form is in Equation 4.5.

$$\begin{aligned}
\hat{x}_{\rm p} &= \cos\delta^{\rm x}_{\rm p}\cos\alpha^{\rm x}_{\rm p}\hat{x}_{\rm eq} + \cos\delta^{\rm x}_{\rm p}\sin\alpha^{\rm x}_{\rm p}\hat{y}_{\rm eq} + \sin\delta^{\rm x}_{\rm zn}\hat{z}_{\rm eq} \\
\hat{z}_{\rm p} &= \cos\delta^{\rm z}_{\rm p}\cos\alpha^{\rm z}_{\rm p}\hat{x}_{\rm eq} + \cos\delta^{\rm z}_{\rm p}\sin\alpha^{\rm z}_{\rm p}\hat{y}_{\rm eq} + \sin\delta^{\rm z}_{\rm zn}\hat{z}_{\rm eq} \\
\hat{y}_{\rm p} &= \hat{z}_{\rm p}\times\hat{x}_{\rm p}
\end{aligned} \tag{4.4}$$

$$\hat{r}_{\rm p} \equiv T_{\rm eq\to p}(\delta^{\rm x}_{\rm p}, \alpha^{\rm x}_{\rm p}, \delta^{\rm z}_{\rm p}, \alpha^{\rm z}_{\rm p})\hat{r}_{\rm eq} \tag{4.5}$$

Similarly, $T_{\rm eq\to p}$ is also considered as a transformation matrix.

The LAT coordinate system is defined such that $\hat{z}_{\rm p}$ points along the boresight and $\hat{x}_{\rm p}$ points along with one of its solar panels. The directions of $\hat{x}_{\rm p}$ and $\hat{z}_{\rm p}$ are also recorded in the equatorial system. Figure 4.3 shows the relationship between the sp and zn coordinate systems.

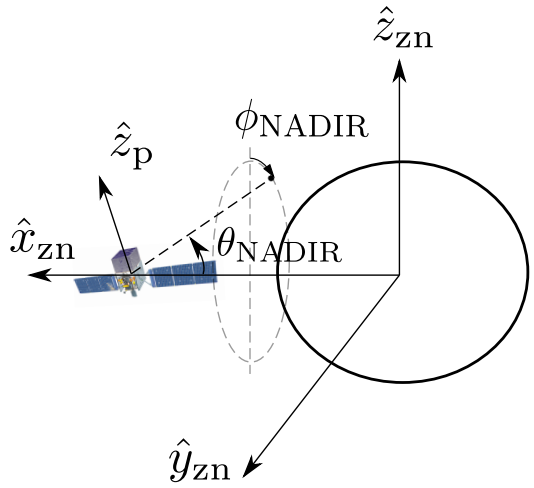

Figure 4.3: Illustration of the local zenith (zn) and the plane of detector (p) coordinate systems. The nadir ($\theta_{\rm NADIR}$) and azimuthal ($\phi_{\rm NADIR}$) angles of a pixel of interest are also shown.

With the two transformation matrices, $T_{\rm eq\to zn}$ and $T_{\rm zn\to p}$, we can transform the position of a pixel in a local zenith coordinate map into the LAT coordinate system to obtain the effective area for that pixel. The exposure for that pixel is the sum of effective are $\times$ lifetime. The spacecraft coordinate can be written as a dependency of Earth's polar coordinate as Equation 4.2.1 in the cartesian system.

$$\hat{r}_{\rm zn}(\theta_{\rm NADIR}, \phi_{\rm NADIR}) \equiv -\cos\theta_{\rm NADIR}\hat{x}_{\rm zn} + \sin\theta_{\rm NADIR}\sin\phi_{\rm NADIR}\hat{y}_{\rm zn} + \sin\theta_{\rm NADIR}\cos\phi_{\rm NADIR}\hat{z}_{\rm zn}$$

Extracting the relations to simplify the LAT's boresight coordinate could be contained by one inversion of transformation matrix from equatorial to spacecraft and transform it to plane of the detector as written in the compact form in Equation 4.6.

$$\hat{r}_{\rm p}(\theta_{\rm N}, \phi_{\rm N}) = T_{\rm eq\to p}(\delta^{\rm x}_{\rm p}, \alpha^{\rm x}_{\rm p}, \delta^{\rm z}_{\rm p}, \alpha^{\rm z}_{\rm p})\left[T_{\rm eq\to zn}(\delta_{\rm zn}, \alpha_{\rm zn})\right]^{-1}\hat{r}_{\rm zn}(\theta_{\rm NADIR}, \phi_{\rm NADIR}) \quad (4.6)$$

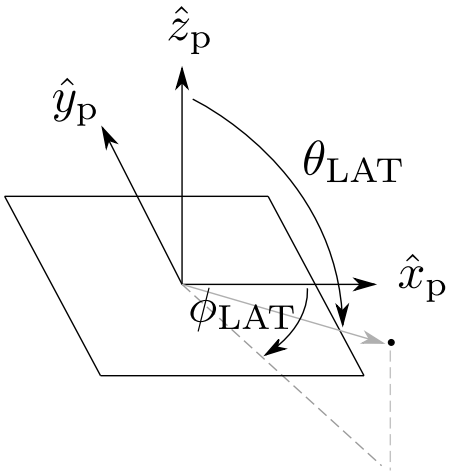

Figure 4.4: A vector pointing to a pixel of interest (grey arrow) in the plane of detector (p) coordinates. The $\hat{z}_{\rm p}$ axis points along the LAT's boresight and the $\hat{x}_{\rm p}$ axis points along with one of its solar panels.

Geometrically, an angular coordinate of the LAT plane could be obtained from a normalized component of the cartesian unit vector as in Figure 4.4. The exposure accumulation has been calculated in every single grid from the previous relation.

Parallel computations

The complexity of the code becomes large due to the transformation operation. For example, a plain matrix inversion cost $\mathcal{O}(n^3)$ where n is 3 because

it is a 3 by 3 matrix in this case. The matrix multiplication also costs the same amount of complexity, rendering exposure map calculation a very computationally intensive task.

The spacecraft files, which contain the information of the LAT position, orientation, and status in rows of the 30-second time step, are called the FT2 files. We use 25 energy bins per decade, so the bin width is small enough to use the geometric mean to represent the mean energy for each bin. Moreover, the exposure maps can be calculated separately for a given time period. We can therefore split the 9-year analysis time into many small time periods, calculate the exposure maps for each time period in parallel, and sum all periods to obtain the total exposure maps.

The code is implemented in Message Passing Interface (MPI). The framework provides a simple protocol for communication between each process with a customizable message schema. It assists the user to freely control multiple processes with full control of each process. According to Flynn's taxonomy of computation, this work exploits the Multiple Instruction Multiple Data (MIMD) architecture to utilize the resources in a distributed system.

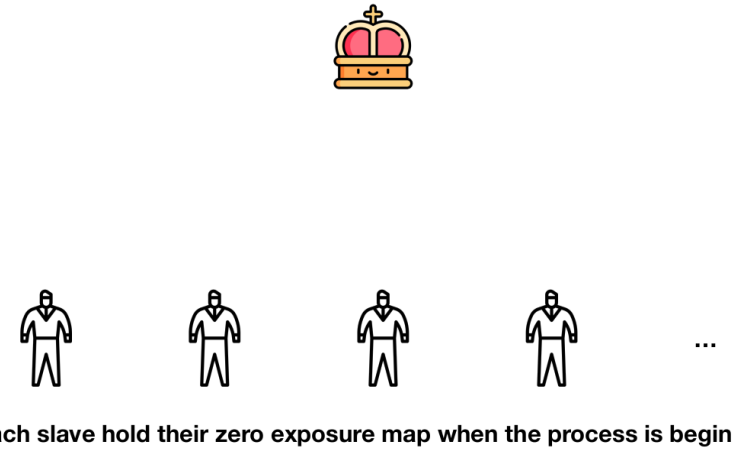

Figure 4.5: Spawning the king and slave processes

In the normal parallel computing setup, sending equal amount of task to each node is not optimized since there would be fast and slow nodes with different performances. Some trivial tasks can lock resources in a computing cluster and

blocks the resource allocation for other tasks. To maximize the usage of the CPU-based cluster computing, there is a mechanism called the "Master-Slave technique". The algorithm has been designed for utilizing the resource by spawning a king as the process manager and multiple slaves to be process workers. The starting process could be demonstrated in Figure 4.5.

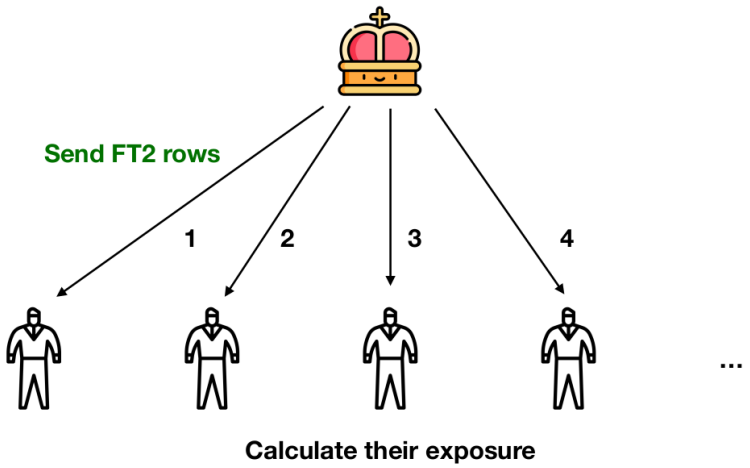

Figure 4.6: Master process sends a small task to slaves.

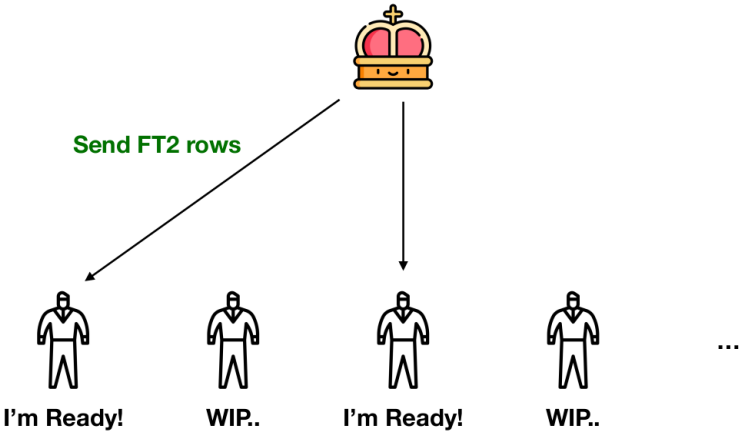

Figure 4.7: Asynchronous assignment of tasks to available slaves.

A certain amount of spacecraft information (FT2 rows) would be sent as an input to slaves sequentially until all slaves are assigned with a small task and start the calculation. There are metadata attached to the message. One of the options is the status tag which let the slaves declare the status of a process

whether it is still in process or has finished. Figure 4.7 illustrates the non-sequential assignment of the workload. Small tasks are sent to available slaves and skip busy slaves. This mechanism allows the execution to utilize the resource in the cluster without wasting free slaves. After all tasks are assigned, the master process will send a status tag announcing that the overall calculation has finished. Then, the exposure maps from all slaves would be added to obtain the final total exposure maps. The benchmark for the calculation time of serial code and parallel code is reported in Appendix A.

4.3 Hadronic collision model

CR spectrum is well described in power in ridigity where the ridigity is a momentum per charge of the particle. The explicit formula for proton power-law spectrum in rigidity in Equation 4.7 as a single power law (SPL) where Γ represents the spectral index of the model. Converting between the ridigity (R) and the energy spectrum is derived in Appendix B.

Single power law (SPL)

$$\frac{dN}{dR} = R_0 R^{-\Gamma} \tag{4.7}$$

where R_0 is the coefficient of the power law. The most crucial part of this work is to determine if there is any breaking in the spectral index of the power law. To represent single breaking energy, the broken power law (BPL) could be modeled by Equation 4.8.

Broken power law (BPL)

$$\frac{dN}{dR} = \begin{cases} R_0 R^{-\Gamma_1} & : \ E < E_{\text{Break}} \\ R_0 [R(E_{\text{Break}})]^{\Gamma_2 - \Gamma_1} R^{-\Gamma_2} & : \ E \geq E_{\text{Break}} \end{cases} \tag{4.8}$$

The collision from incoming protons with kinetic energy above 10 GeV striking the Earth's atmosphere be modeled by proton-proton collision with a thin-target where the scaling of normalization depending on the chemical composition ~~of the air.~~ The proton-proton collision yielding γ rays as secondary products for a

broad and smooth spectrum of proton can be modeled by Equation 4.9 taken from Kachelrieß & Ostapchenko (2012) as

$$\frac{dN_\gamma}{dE_\gamma} \propto \int_{E_\gamma}^{E_{\max}} dE' \frac{dN_p}{dE'} \frac{d\sigma^{pp\to\gamma}}{dE_\gamma}(E', E_\gamma), \tag{4.9}$$

where $d\sigma^{pp\to\gamma}(E', E_\gamma)/dE_\gamma$ contains the scattering amplitude for the kinetic energy of proton E' and the energy of γ ray E_γ. Atmospheric components mostly consists of nitrogen as the majority and the oxygen (Wallace & Hobbs 2006). ~~The cross-section from proton-proton collision and proton-nitrogen collision is roughly approximate as the multiplicative relation since there is the plateau curve in the energy range in this analysis.~~ The relation of the proton-proton scattering amplitude and the proton-air is obtained from Atwater & Freier (1986a) where it highly depends on the atomic numbers of the air molecules.

However, the second highest fraction of the arrival CR particles on Earth is ~~an~~ alpha (α) particle. ~~The helium nuclei can interact with the nitrogen and produce high energy γ-rays depends on how much kinetic energy α-particles is holding.~~ Another estimation has been exploited by applying $\sigma_{\alpha N}/\sigma_{pN}$ to be a constant around 1.6 at the energy range in GeV from the same relationship of the proton-air collision model. Hence, derived equation of the scattering process from incoming proton and α-particle with air molecules to produce γ-ray spectrum could be shown as Equation 4.10

$$\frac{dN_\gamma}{dE_\gamma}(E_\gamma) \propto \sum_{E_i'} \left[\frac{E_i'}{E_\gamma}\Delta(\ln E_i')\right] \left[f_{pp}\frac{dN_p}{dE_i'}\left\{1 + \frac{\sigma_{\mathrm{HeN}}}{\sigma_{p\mathrm{N}}}\left(\frac{dN_p}{dR}\right)^{-1}\frac{dN_{\mathrm{He}}}{dR}\frac{dR_{\mathrm{He}}}{dR_p}\right\}\right], \tag{4.10}$$

The CR helium spectrum would not be measured in this work since there will be multiple parameters that lead to an overwhelming local optimum. The spectrum of α-particles is directly measured by Aguilar et al. (2015) and fix the distribution as one function rather than modeled spectrum of CR proton spectrum. The full detail of the equation derivation will be demonstrated in D.

4.4 Optimization

Determining the best-fit spectral model requires an objectives function to represent how well the model match with an observed data. A proper methodology for fitting or optimization in another word is also a crucial part since it is likely that the local optimum exists in the parameters space. A poor optimization could lead the best-fit stuck in a local minimum and yield a poor result. For better escaping local optima, heuristic optimization is employed for finding the best-fit of the model in parameter space.

Poisson likelihood function

An objective function is defined as Poisson likelihood function in the Equation 4.11. The reason behind the selection of the Poisson function came from the observed model and measurement is considered as a number of photons in each bin of the histogram. Converting the model spectrum to be a count histogram is simply multiplied by the integral of the exposure map in the limb region.

$$\mathcal{L} = \prod_{i=1}^{N} P_{\text{pois}}(n_{\text{i,model}}, n_{\text{i,measurement}}) \tag{4.11}$$

Since the spectrum order is in different order of magnitude, then a proper way to define an objective function is to redefine a likelihood as a log-likelihood function for numerically convenient like Eq 4.12.

$$Sum = \sum_{i=1}^{N} - \log P_{\text{pois}}(n_{\text{i,model}}, n_{\text{i,measurement}}) \tag{4.12}$$

To sum up, a given proton spectrum yield a distribution of γ-ray spectrum to be converted into a count histogram and comparing with the real measurement. Not only for numerical convenience but the negative sign also makes an algorithm to minimize the system rather than maximize a likelihood.

Particle Swarm Optimization (PSO)

In the early phase of the optimization, a plain gradient descent optimization has been used for model fitting. The result turns out that with different initial

parameters, the different best-fit model has changed which implies the local minimum in the problem. Even there is no method to guarantee the global minimum but the heuristic optimization could be a better option for handling this type of problem. One kind of most widely used algorithm is particle swarm optimization (PSO) and it is invented by Kennedy & Eberhart (1995).

In order to get a best fit spectral indices, employing the Particle Swarm Optimization (PSO) by randomly initiate many particles in a given range of the parameter space and find the local and global best fit in each step of the iteration. Then rest of them would slowly move toward to the local and global position in parameter space with a proper weight. The iteration process will stop when the standard deviation of the objective function from every particle less than a decimal. The explicit formula for every iteration k, particle i move with velocity v_k^i is

$$v_{k+1}^i = \omega v_k^i + c^b r_k^b [b_k^i - x_k^i] + c^B r_k^B [B_k^i - x_k^i], \tag{4.13}$$

and updating the particle i with

$$x_{k+1}^i = x_k^i + v_{k+1}^i. \tag{4.14}$$

where

- ~~x_k^i represent variable that particle i hold~~
- b and B are best local and global parameter sets along the optimization process
- Set $\omega = 0.2$, $c^b = 0.2$ and $c^B = 0.3$

4.5 Statistical significance

Certainly, larger model parameters or complexity would yield a better performance except it is overfitting the problem. The critical issue is to answer how much significance the alternative model could outperform the trivial model. ~~As the language of statistics would consider as two hypotheses. One for null and one for an alternative approach.~~

For this case, BPL has 2 more degrees of freedom (DOF) than SPL. ~~Unquestionably, if there is a good optimization procedure, the objectives function would say BPL is better SPL. As mentioned in the previous paragraph, the significance level has to be taken into account to put the weight on the study.~~ Theoretically, regarding the model likelihood with a given set of parameters could be determined in the general case as Wilk's theorem define the relation in Equation 4.15.

$$\mathcal{L} \equiv \prod_{\alpha=1}^{n} f(x_\alpha, \theta_1, \theta_2, ..., \theta_h) \tag{4.15}$$

where

- x_α is represent a variant from model and data
- θ_i is a degree of freedom (DOF)

The practical usage to compare the null hypothesis and the alternative hypothesis is similar to one-tail hypothesis testing with a given dependency in more DOF has been adopted by Huelsenbeck & Crandall (1997). This method called "Likelihood ratio test (LRT)". The compact formula is ~~shown in Equation 4.16.~~

$$\text{LRT} = -2\ln\left(\frac{\mathcal{L}_{\text{null}}}{\mathcal{L}_{\text{alternative}}}\right) \tag{4.16}$$

CHAPTER V
RESULTS AND DISCUSSION

The content of this chapter would be reported as the analysis procedure from step one to the end. ~~The first part is the~~ data correction process, count maps from the raw count as well as exposure map from the parallel computation, the spectrum and inversive fitting from heuristic optimization.

5.1 Limb angle correction

~~Theoretically, the peak profile of the~~ θ_{NADIR} ~~would be the same when time passes by.~~ From the observations, the nadir angle change through time evolving since the spacecraft altitude is gradually getting lower each year which will affect the LAT point of view when it sees the Earth.

The top-left of Figure 5.1 demonstrates how ~~much~~ spacecraft orbiting altitude correlates to the θ_{NADIR} by a 2D heatmap plot of photon intensity. The bottom-left histogram came from the projection of the previous raw count 2-D histogram which has a peak around 68°. Both bottom and top right histograms were constructed from the same logic but there is one different variable. The shifted nadir angle has been calculated to reduce the effect from the spacecraft and the region of interest has been highlighted as orange for calculating as the limb spectrum and the blue zone is a diffusive background to be used in the background subtraction.

~~The brightness of Earth's limb is much brighter than the diffusive background on the map. The region of interest and the background intensity has a huge difference in approximately an order of magnitude.~~

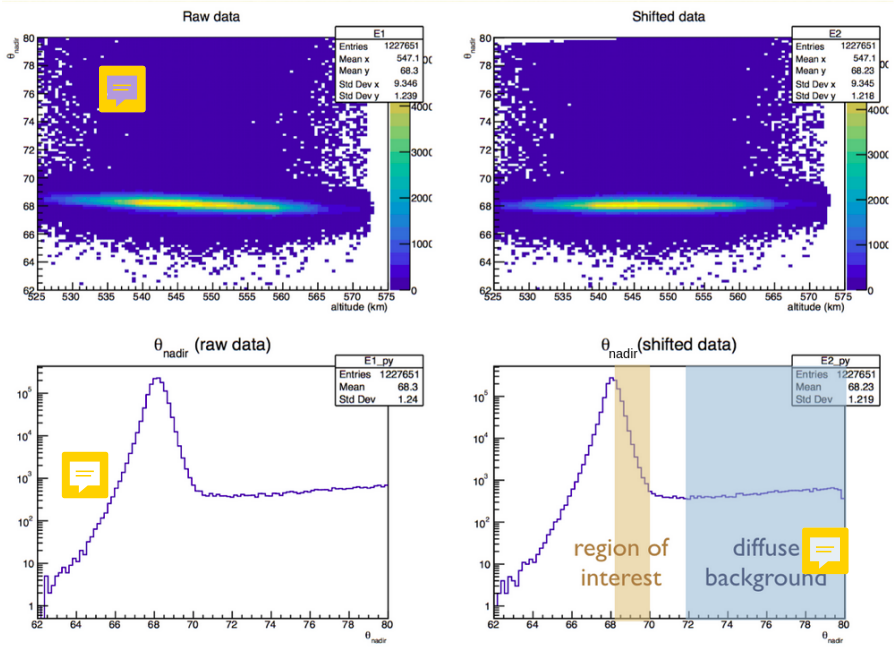

Figure 5.1: Distribution of nadir angle before and after altitude correction. (top) Heatmaps represents the photon density in axis of θ_{NADIR} versus altitude in kilometers. ~~The left one came from raw data and the right one was converted by altitude shifting calculation.~~ ~~(bottom)~~ The projected histograms from the above heatmaps in the axis of θ_{NADIR} where all photon from various altitudes was accumulated into the bin value.

5.2 γ-ray spectrum measurement

According to ~~the definition from~~ Equation 4.1, the first step is the construction of the count map of the Earth's centered coordinates. To illustrate how the outcome looks like, we selected photon data from a single week due to the raw data of photon from *Fermi* was published once a week as one file. A week of the accumulated photons is plotted in Figure 5.2 to visualize the raw count of the sample data on the count map.

The limb's region could be easily observed in the bright ring above a dashed line at $\theta_{\mathrm{NADIR}} = 60°$. Figure 5.2 also shows the brightness of the southern and northern hemispheres. Further investigating of the East-West effects could be illustrated by projecting the 2-D histogram into a 1-D histogram of the nadir angle as in Figure 5.2b. Nevertheless, the explanation of the East-West is a rough description and still incomplete because it does not take the exposure into account yet.

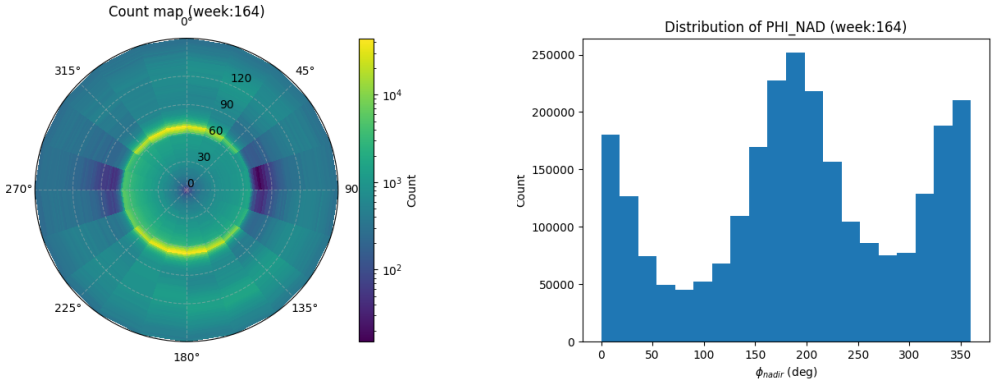

(a) Heatmap of photon density in nadir angle where the radius direction is the azimuthal nadir angle (θ_{NADIR}). (b) A projected histogram from the heatmap. The x-axis is ϕ_{NADIR} from 0°to 360°.

Figure 5.2: An example distribution of γ-ray from a single week.

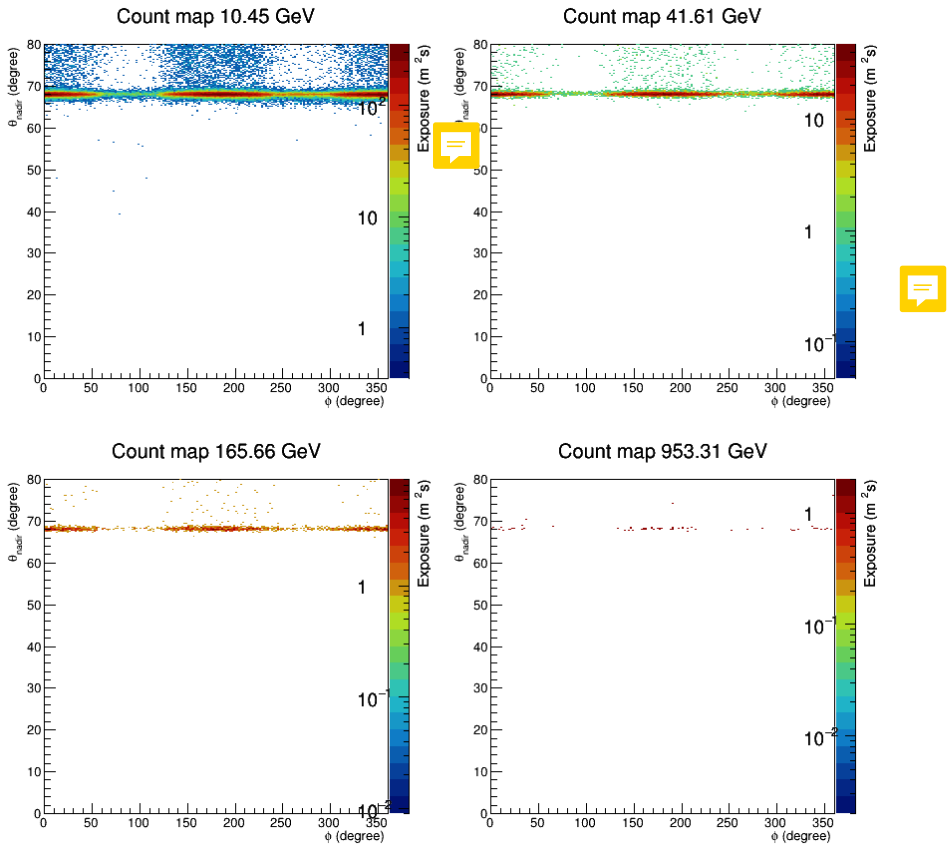

~~Figure 5.3: Cartesian plot of the γ-ray count histograms. The title each sub-figure represents mean of the energy bins.~~

~~Since the final spectrum will contain 50 energy bins with their specific energy range and mean energy for each energy bin. In practice, each heatmap will~~

be constructed for their belonging bin of the histogram in the energy domain as in Figure 5.3.

However, inspecting at polar coordinate plotting from the cartesian point of view might not be the best option for illustration since it not looks like the real orientations. Figure 5.4 is another angle of viewing the same data but in more natural orientations. Both visualizations show that the Earth's limb region in γ-ray is the shinest band for all interesting energy. It is also obvious to say that the higher energy scale, the less photon appears after applying criteria.

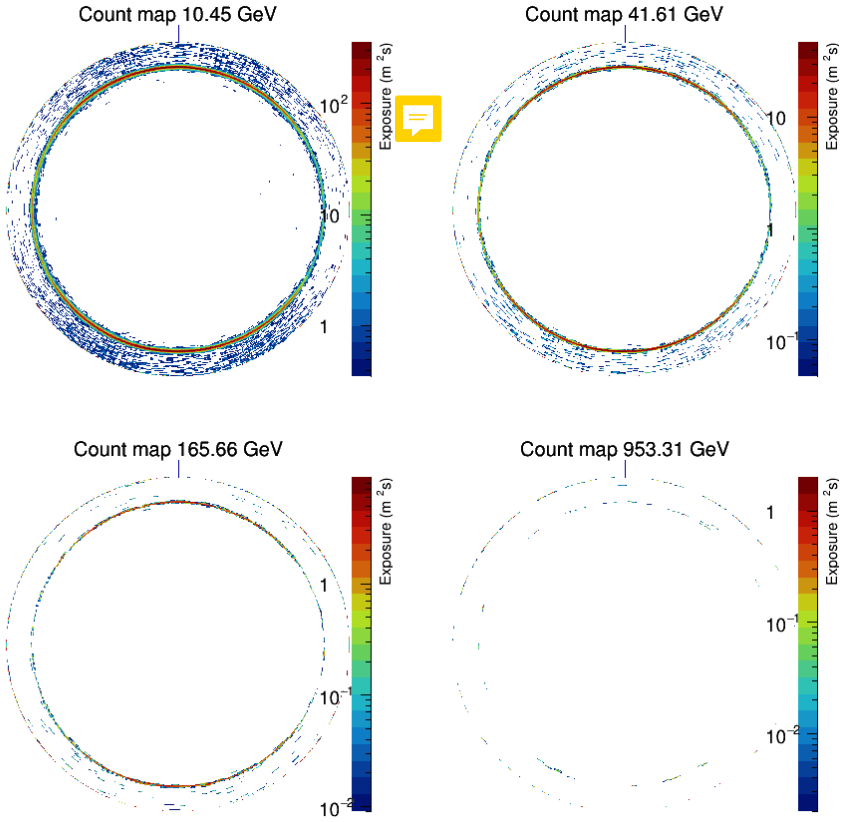

Figure 5.4: Polar plot of the γ-ray count histograms.

The next step is the exposure calculation. The exposure map is computed by accumulating exposure time from the LAT's FoV in each step time as well as takes the effectiveness of the detector due to incident angle affects the performance of the detector. A unit from the calculation will be an area multiple by the time. Raw cartesian plots are visualized in Figure 5.5 with an attached axis.

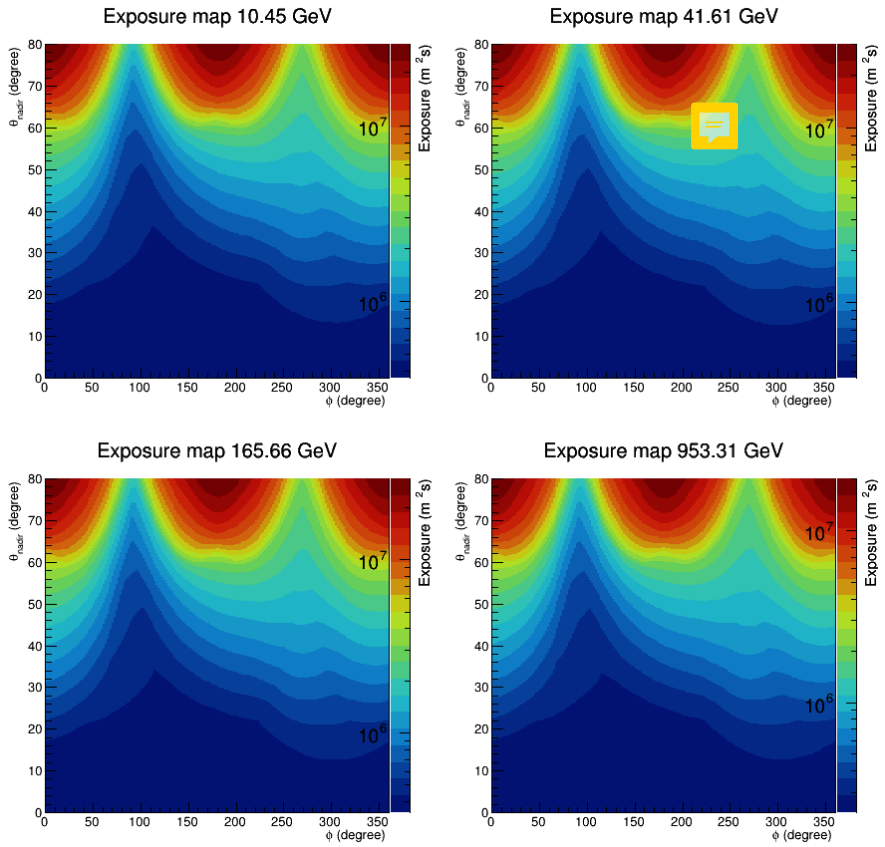

Figure 5.5: Cartesian plot of the exposure histograms.

The exposure intensity in the sky is much higher than the Earth in an order of magnitude because *Fermi* was designed for seeking flare events in space rather than the Earth. Regarding a given nadir angle between 60°to 70 °, the spacecraft seems to look at the northern and southern hemispheres more than the eastern and the western side. The color of the at 270°(West) is more intense than 90°(East) means that the spacecraft tends to peek in the Westside more than Eastside. ~~The reason might come from the trajectory of the charged particles was bent and produce a γ-ray which potentially could convince *Fermi* to look at them rather than the other side because it has a more for triggering the GBM. The 2-D histograms in polar coordinates have also been plotted in Figure 5.6.~~

The last step starts with initiating the new heatmaps that were defined by the element-wise division from the count maps and the exposure maps. ~~After that, integrating the limb region in the polar coordinates to get a single scalar~~

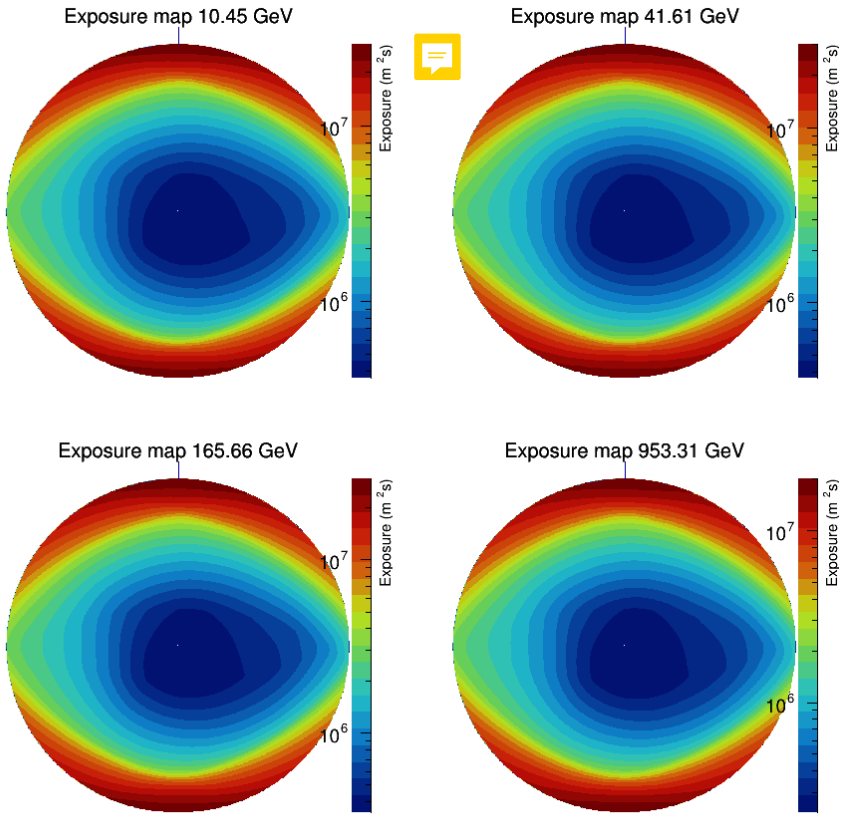

Figure 5.6: Polar plot of the exposure histograms.

value. The scalar is then divided by the gap of the energy bin and the solid angle. Repeating the above process for 50 energy bins in the γ-ray spectrum and subtracts by the background would yield the final photon spectrum as in Figure 5.7.

In addition, exploring the γ-ray intensity from the visualization of the Earth's centered coordinates would be informative aspects to observe the variation of the photon intensity along the nadir angle as well as the East-West effect. The cartesian plotted as in Figure 5.8 and the polar form as in the Figure 5.9. ~~Comparing the intensity along the peak of theta nadir in the cartesian plot from the East (ϕ=90°) and West (ϕ=270°) would reflect that the band of the intensity in the west is slightly thicker than in the East and the color of the peak center is more a little darker than the other side.~~ It means that not only the intensity but also the ring thickness of the limb region is larger from West to East.

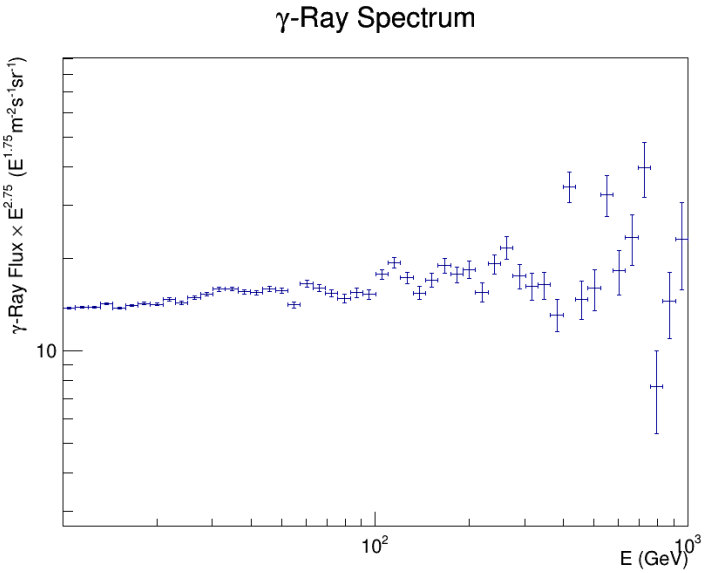

Figure 5.7: Measured γ-ray spectrum.

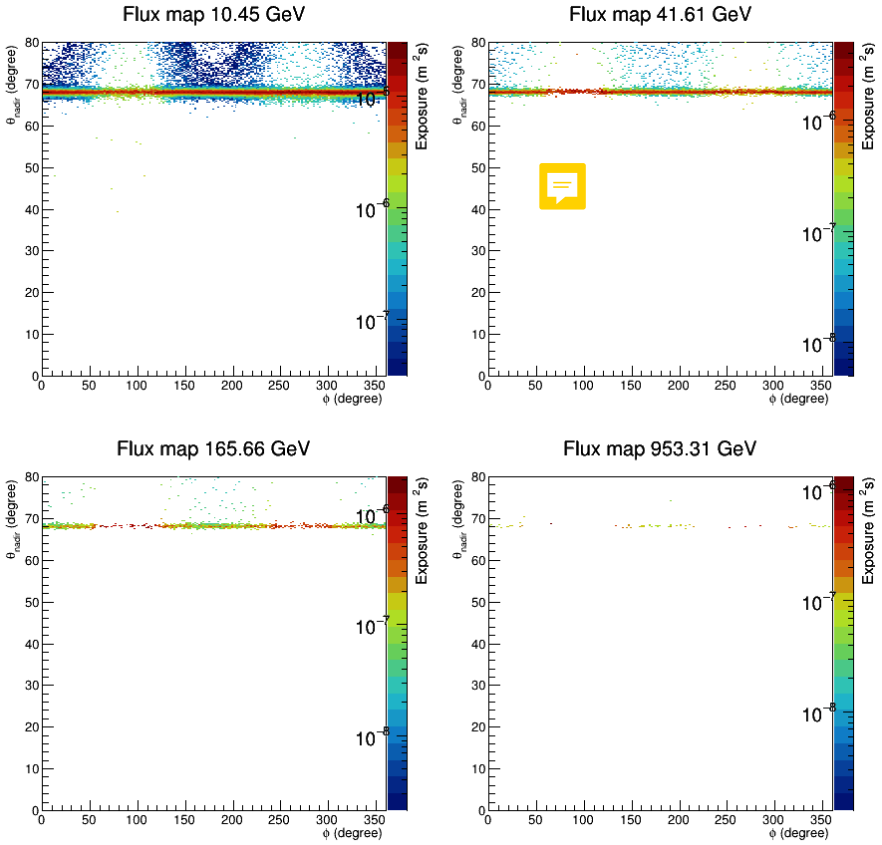

Figure 5.8: Cartesian plot of the γ-ray flux histograms.

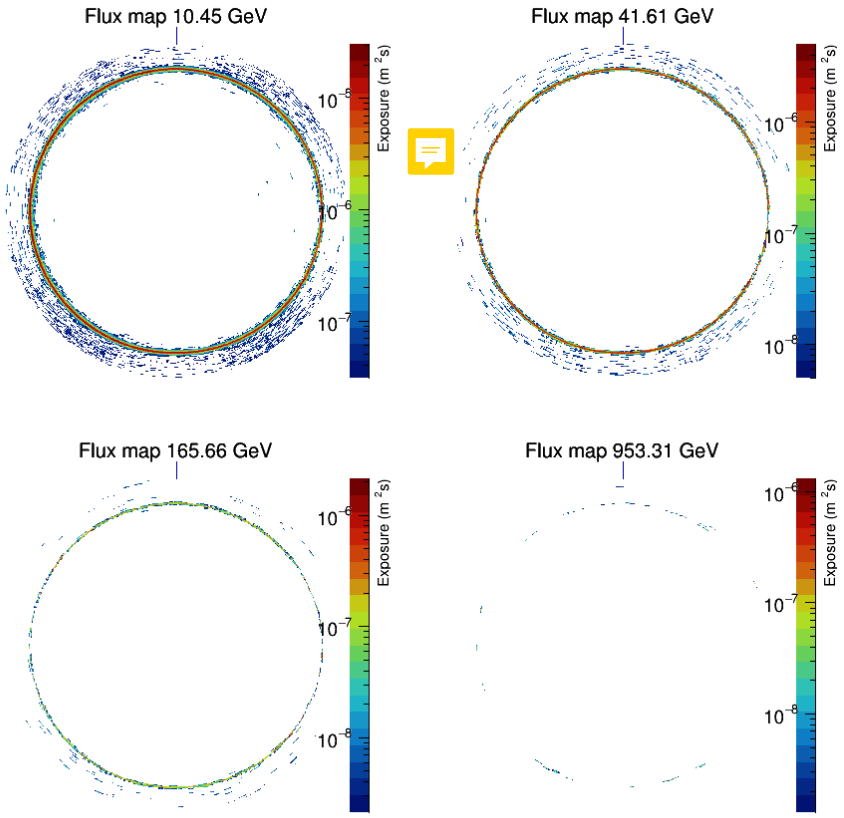

Figure 5.9: Polar plot of the γ-ray flux histograms.

5.3 Best fit result

The optimized parameters for Single Power Law (SPL) and Broken Power Law (BPL) models are summarized in Table 5.1. Best fit γ-ray from both models is visualized in Figure 5.10 along with the spectrum from the measurement. The result shows the consistency between the direct measurement from AMS-02 and the previous work. Both studies identify the breaking point of the spectral index in proton spectrum at $\sim$ 300 GeV, as well as the previous work, reported $\Gamma_1 \sim 2.81$ and $\Gamma_2 \sim 2.68$ for the BPL model.

Best fits	Γ_1	Γ_2	E_{Break} (GeV)
SPL	2.70	-	-
BPL	2.86	2.63	333

Table 5.1: Optimization results.

~~The comparative illustration also is visualized in Figure 5.11 with a~~

~~scaled spectrum from both models to collate two other direct observations of the space-based experiments. It is obvious to see the consistency of BPL with the direct measurements in the bellowing sub-figure is more corresponding than the SPL model in the top sub-figure because the breaking point of the BPL does looks more likely to be a proper model where the x-axis is the same rigidity scale.~~

However, a more complex model would perform better than the model that has less degree of freedom in practice. Determining the statistical significance would be the best way to answer whether CR spectrum is naturally described as a BPL indeed. The significant level could be determined by taking the outcome from the objective function to Equation 4.16 for testing one-tail hypothesis-like from the null hypothesis comparing to an alternative hypothesis which is the model of breaking of spectral indices, or SPL versus BPL in other words. The significance is around 1.38σ or at 92% confidence level.

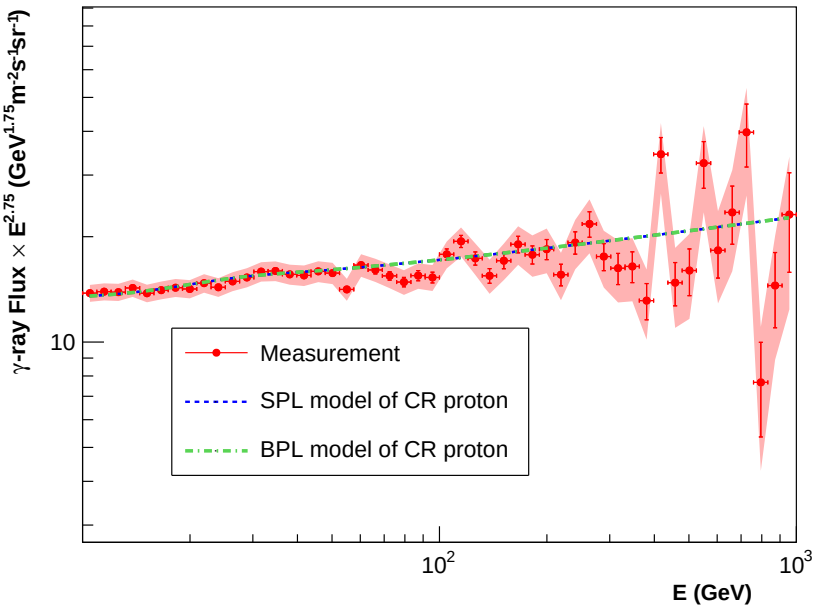

Figure 5.10: The γ-ray spectra calculated from the SPL (blue) and BPL (red) models of CR proton which best fit with the measured ~~Earth's γ-ray~~ spectrum in the thin-target regime (red).

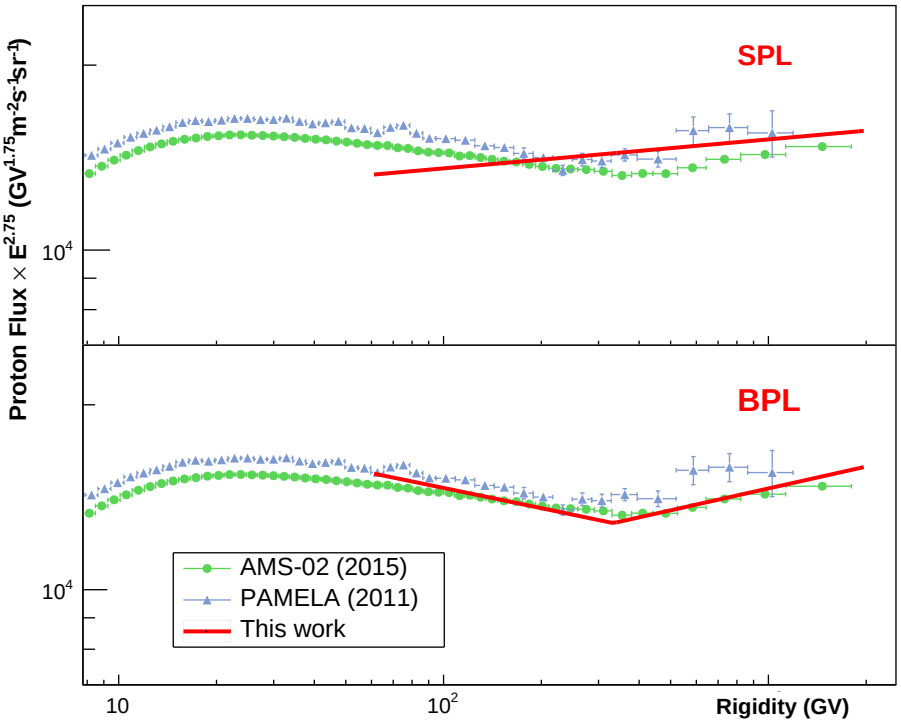

Figure 5.11: Best-fit CR proton spectrum from this work (red) compared to the measurementsby AMS-02 (blue) and PAMELA (green).

CHAPTER VI
CONCLUSION

In this study, the incident CR proton spectrum was tracing by using the limb γ-ray. The measured γ-ray spectrum is constructing by taking the exposure of the LAT and the effective area into account where on the Earth-centered coordinates. The exposure calculation is calculated from the relation of the angle between the LAT's boresight and nadir angle because given nadir angle and the spacecraft orientation affects the performance of the measurement. After that, an indirect measurement of the proton spectrum was inversely computed via the $pp \rightarrow \gamma$ interaction model with a heuristic optimization technique.

~~Since the *Fermi*-LAT was launched in June 2008. The data that has been used in this analysis starting from 7 August 2008 to 16 October 2017. The collection from 9 years of observations was recorded for both γ-rays data and the spacecraft orientation logging. The LAT mostly observing the sky and looking for a flare of γ-rays. However, there is a moment that LAT FoV can see the Earth or even stare at the Earth for some reason. Filtering photons from the Earth's limb region was done by selecting an incoming photon in the direction between 68.4°-70°nadir angle with the cleanest event class.~~

To sum up, a statistical significance from the analysis yields 1.38σ. ~~Meaning that there is a confidence level of breaking spectrum in CR proton at 92%. This level of significance is still now strong for confirmation.~~ Nevertheless, the previous study with a few data collection periods gives 1.0σ significant level. ~~It implicitly tells that the larger data collection could increase the statistics and put the weight on the previous study.~~ Surprisingly, the direct CR proton measurement from AMS-02 identifies a breaking spectrum at 340 GV which is very close to our work. There is also one plausible assumption where the indirect measurement could not yield a strong significant even have a huge amount of data.

REFERENCES

1. Abdo, A. A., Ackermann, M., Ajello, M., Atwood, W. B., Baldini, L., Ballet, J., et al. (2009). Fermi large area telescope observations of the cosmic-ray induced γ-ray emission of the earth's atmosphere. *Phys. Rev. D*, 80, 122004.
2. Abdo, A. A., Ackermann, M., Ajello, M., Atwood, W. B., Baldini, L., Ballet, J., et al. (2009). Fermi large area telescope observations of the cosmic-ray induced γ-ray emission of the Earth's atmosphere. *Physical Review D*, 80(12), 122004.
3. Abraham, J., Abreu, P., Aglietta, M., Ahn, E., Allard, D., Allen, J., et al. (2010). Measurement of the energy spectrum of cosmic rays above 1018 ev using the pierre auger observatory. *Physics Letters B*, 685(4-5), 239–246.
4. Ackermann, M., Ajello, M., Albert, A., Allafort, A., Baldini, L., Barbiellini, G., et al. (2014). Inferred Cosmic-Ray Spectrum from Fermi Large Area Telescope γ-Ray Observations of Earth's Limb. *Physical Review Letters*, 112(15), 151103.
5. Ackermann, M., Ajello, M., Allafort, A., Atwood, W. B., Baldini, L., Barbiellini, G., et al. (2012). Measurement of Separate Cosmic-Ray Electron and Positron Spectra with the Fermi Large Area Telescope. *Physical Review Letters*, 108(1), 011103.
6. Adriani, O., Barbarino, G., Bazilevskaya, G., Bellotti, R., Boezio, M., Bogomolov, E., et al. (2009). An anomalous positron abundance in cosmic rays with energies 1.5–100 gev. *Nature*, 458(7238), 607–609.
7. Adriani, O., Barbarino, G., Bazilevskaya, G., Bellotti, R., Boezio, M., Bogomolov, E., et al. (2011). Pamela measurements of cosmic-ray proton and helium spectra. *Science*, 332(6025), 69–72.
8. Aguilar, M., Aisa, D., Alpat, B., Alvino, A., Ambrosi, G., Andeen, K., et al.

(2015). Precision Measurement of the Helium Flux in Primary Cosmic Rays of Rigidities 1.9 GV to 3 TV with the Alpha Magnetic Spectrometer on the International Space Station. *Physical Review Letters*, 115(21), 211101.

9. Aguilar, M., Aisa, D., Alpat, B., Alvino, A., Ambrosi, G., Andeen, K., et al. (2015). Precision measurement of the helium flux in primary cosmic rays of rigidities 1.9 gv to 3 tv with the alpha magnetic spectrometer on the international space station. *Phys. Rev. Lett.*, 115, 211101.
10. Aguilar, M., Aisa, D., Alpat, B., Alvino, A., Ambrosi, G., Andeen, K., et al. (2015). Precision Measurement of the Proton Flux in Primary Cosmic Rays from Rigidity 1 GV to 1.8 TV with the Alpha Magnetic Spectrometer on the International Space Station. *Physical Review Letters*, 114(17), 171103.
11. Amsler, C., et al. (2008). Particle data group. *Phys. Lett. B*, 667(1).
12. Atwater, T. W., & Freier, P. S. (1986a). Meson multiplicity versus energy in relativistic nucleus-nucleus collisions. *Phys. Rev. Lett.*, 56, 1350–1353.
13. Atwater, T. W., & Freier, P. S. (1986b). Meson multiplicity versus energy in relativistic nucleus-nucleus collisions. *Physical review letters*, 56(13), 1350.
14. Atwood, W., Albert, A., Baldini, L., Tinivella, M., Bregeon, J., Pesce-Rollins, M., et al. (2013). Pass 8: Toward the Full Realization of the Fermi-LAT Scientific Potential. *arXiv e-prints*, arXiv:1303.3514.
15. Atwood, W. B., Abdo, A. A., Ackermann, M., Althouse, W., Anderson, B., Axelsson, M., et al. (2009). The Large Area Telescope on the Fermi Gamma-Ray Space Telescope Mission. *The Astrophysical Journal*, 697, 1071–1102.
16. B., R., Ütikofer, E.O., F., & LÜCKIGER (2007). 30th international cosmic ray conference characteristics of near real-time cutoff calculations on a local and global scale.
17. Baldini, L. (2014). Space-based cosmic-ray and gamma-ray detectors: a review. *arXiv preprint arXiv:1407.7631*.

18. Becquerel, H. (1896). On the rays emitted by phosphorescence. *Compt. Rend. Hebd. Seances Acad. Sci.*, 122(8), 420–421.

19. Belolaptikov, I., Budnev, N., Sinegovsky, S., Padusenko, A., Wiebusch, C., Moroz, A., et al. (1997). The baikal underwater neutrino telescope: Design, performance and first results. Tech. rep., SCAN-9704016.

20. Beringer, J., Arguin, J. F., Barnett, R. M., Copic, K., Dahl, O., Groom, D. E., et al. (2012). Review of particle physics. *Phys. Rev. D*, 86, 010001.

21. Bird, D., Corbato, S., Dai, H., Dawson, B., Elbert, J., Emerson, B., et al. (1994). The cosmic-ray energy spectrum observed by the fly's eye. *The Astrophysical Journal*, 424, 491–502.

22. Carlson, A., Hooper, J., & King, D. (1950). Lxiii. nuclear transmutations produced by cosmic-ray particles of great energy.-*Part V.* the neutral mesons. *Philosophical Magazine Series 7*, 41(318), 701–724.

23. Clay, J. (1927). Penetrating Radiation I. In Proceedings of the Royal Academy of Sciences Amsterdam. vol. 30, pp. 1115–1127.

24. Clay, J. (1928). Penetrating Radiation II. In Proceedings of the Royal Academy of Sciences Amsterdam. vol. 31, pp. 1091–1097.

25. Compton, A. H., & Turner, R. (1937). Cosmic rays on the pacific ocean. *Physical Review*, 52(8), 799.

26. Curie, M. (1923). Pierre Curie. Macmillan.

27. De Angelis, A. (2014). Atmospheric ionization and cosmic rays: studies and measurements before 1912. *Astroparticle Physics*, 53, 19–26.

28. Dembinski, H. P., Engel, R., Fedynitch, A., Gaisser, T., Riehn, F., & Stanev, T. (2017). Data-driven model of the cosmic-ray flux and mass composition from 10 GeV to \$10ˆ{11}\$ GeV. In Proceedings of 35th International Cosmic Ray Conference — PoS(ICRC2017). Sissa Medialab.

29. Dermer, C. D., & Powale, G. (2013). Gamma rays from cosmic rays in supernova remnants. *Astronomy & Astrophysics*, 553, A34.

30. Dorman, L. (2009). First measurements of cosmic ray geomagnetic effects and the problem of CR nature. In Astrophysics and Space Science Library, Springer Netherlands. pp. 1–8.

31. Dorman, L. I., Fedchenko, S. G., Granitsky, L. V., & Rishe, G. A. (1970). Coupling and barometer coefficients for measurements of cosmic ray variations at altitudes of 260-400 mb. In International Cosmic Ray Conference. vol. 2, p. 233.
32. Ertley, C. (2014). Studying the polarization of hard x-ray solar flares with the gamma ray polarimeter experiment (grape).
33. Fermi, E. (1949). On the origin of the cosmic radiation. *Physical review*, 75(8), 1169.
34. Fricke, R. G., & Schlegel, K. (2017). Julius elster and hans geitel-dioscuri of physics and pioneer investigators in atmospheric electricity. *History of Geo-and Space Sciences*, 8(1), 1.
35. Gaisser, T. K., Stanev, T., & Tilav, S. (2013). Cosmic ray energy spectrum from measurements of air showers. *Frontiers of Physics*, 8(6), 748–758.
36. Gerward, L. (1999). Paul villard and his discovery of gamma rays. *Physics in perspective*, 1(4), 367–383.
37. Gray, G. W. (1949). Cosmic rays. *Scientific American*, 180(3), 28–39.
38. Greisen, K. (1966). End to the cosmic-ray spectrum? *Physical Review Letters*, 16(17), 748–750.
39. Haino, S., Sanuki, T., Abe, K., Anraku, K., Asaoka, Y., Fuke, H., et al. (2004). Measurements of primary and atmospheric cosmic-ray spectra with the bess-tev spectrometer. *Physics Letters B*, 594(1-2), 35–46.
40. Halzen, F., & Klein, S. R. (2010). Invited review article: Icecube: an instrument for neutrino astronomy. *Review of Scientific Instruments*, 81(8), 081101.
41. Hess, V. F. (1912). Über beobachtungen der durchdringenden strahlung bei sieben freiballonfahrten. *Phys. Z.*, 13, 1084–1091.
42. Huelsenbeck, J. P., & Crandall, K. A. (1997). Phylogeny estimation and hypothesis testing using maximum likelihood. *Annual Review of Ecology and Systematics*, 28(1), 437–466.
43. Hörandel, J. R. (2013). Early cosmic-ray work published in german. *AIP Conference Proceedings*, 1516(1), 52–60.
44. Isbert, J., Case, G., Granger, D., Guzik, T. G., Price, B., Stewart, M., et al.

(2002). Atic, a Balloon Borne Calorimeter for Cosmic Ray Measurements. In CALORIMETRY IN PARTICLE PHYSICS. Proceedings of the Tenth International Conference. Held 25-29 March 2002 in Pasadena. pp. 89–94.

45. Kachelrieß, M., & Ostapchenko, S. (2012). Deriving the cosmic ray spectrum from gamma-ray observations. *Phys. Rev. D*, 86, 043004.
46. Kelner, S. R., Aharonian, F. A., & Bugayov, V. V. (2006). Energy spectra of gamma rays, electrons, and neutrinos produced at proton-proton interactions in the very high energy regime. *Physical Review D*, 74(3), 034018.
47. Kennedy, J., & Eberhart, R. (1995). Particle swarm optimization. In Proc. of ICNN'95 - Int. Conf. on Neural Networks. Perth, WA, Australia, vol. 4, p. 1942.
48. Kirk, T. B., & Neddermeyer, S. H. (1968). Scattering of high-energy positive and negative muons on electrons. *Physical Review*, 171(5), 1412.
49. Kolhörster, W. (1934). Cosmic rays under 600 metres of water. *Nature*, 133(3359), 419–419.
50. Kraushaar, W., & Clark, G. (1962). Search for primary cosmic gamma rays with the satellite explorer xi. *Physical Review Letters*, 8(3), 106.
51. Kraushaar, W., Clark, G., Garmire, G., Helmken, H., Higbie, P., & Agogino, M. (1965). Explorer xi experiment on cosmic gamma rays. *The Astrophysical Journal*, 141, 845.
52. Kraushaar, W. L., Clark, G. W., Garmire, G. P., Borken, R., Higbie, P., Leong, V., & Thorsos, T. (1972). High-Energy Cosmic Gamma-Ray Observations from the OSO-3 Satellite. *The Astrophysical Journal*, 177, 341.
53. Lesur, V. (2006). Introducing localized constraints in global geomagnetic field modelling. *Earth, planets and space*, 58(4), 477–483.
54. Linsley, J. (1963). Evidence for a primary cosmic-ray particle with energy 10 20 ev. *Physical Review Letters*, 10(4), 146.
55. Madlee, S., Mitthumsiri, W., Ruffolo, D., Digel, S., & Nuntiyakul, W. (2020). First analysis of earth's stratospheric gamma-ray emission in

geographical coordinates with fermi lat. *Journal of Geophysical Research: Space Physics*, 125, 28151.

56. Maldera, S. (2019). Fermi-lat performance,. `https://www.slac.stanford.edu/exp/glast/groups/canda/lat_Performance.htm`. Accessed: 2021-04-19.
57. Michelson, P. F., Atwood, W. B., & Ritz, S. (2010). Fermi gamma-ray space telescope: high-energy results from the first year. *Reports on Progress in Physics*, 73(7), 074901.
58. Millikan, R. A. (1932). Cosmic-ray ionization and electroscope-constants as a function of pressure. *Physical Review*, 39(3), 397.
59. M.J. Berger, J. H. (2010). Xcom: Photon cross sections database. (accessed: 07.06.2018).
60. Morris, D. J. (1984). Production of high-energy gamma rays by cosmic ray interactions in the atmosphere and lunar surface. *Journal of Geophysical Research*, 89, 10685–10696.
61. Morrison, P. (1958). On gamma-ray astronomy. *Il Nuovo Cimento (1955-1965)*, 7(6), 858–865.
62. Neddermeyer, S. H., & Anderson, C. D. (1937). Note on the nature of cosmic-ray particles. *Physical Review*, 51(10), 884.
63. Nuntiyakul, W., Evenson, P., Ruffolo, D., Sáiz, A., Bieber, J. W., Clem, J., et al. (2014). Latitude Survey Investigation of Galactic Cosmic Ray Solar Modulation during 1994-2007. *The Astrophysical Journal*, 795, 11.
64. Orth, C. D., & Buffington, A. (1976). Secondary cosmic-ray electrons and positrons from 1 to 100 gev in the upper atmosphere and interstellar space, and interpretation of a recent positron flux measurement. *The Astrophysical Journal*, 206, 312–332.
65. Petry, D. (2005). The Earth's Gamma-ray Albedo as observed by EGRET. In F. A. Aharonian, H. J. Völk, & D. Horns (Eds.), High Energy Gamma-Ray Astronomy. *American Institute of Physics Conference Series*, vol. 745, pp. 709–714.
66. Rochester, G., & Butler, C. (1953). The new unstable cosmic-ray particles.

Reports on Progress in Physics, 16(1), 364.

67. Rossi, B. (1930). On the Magnetic Deflection of Cosmic Rays. *Physical Review*, 36, 606–606.
68. Rossi, B., & Greisen, K. (1941). Cosmic-ray theory. *Reviews of Modern Physics*, 13(4), 240.
69. Ruffolo, D., Sáiz, A., Mangeard, P.-S., Kamyan, N., Muangha, P., Nutaro, T., et al. (2016). Monitoring Short-term Cosmic-ray Spectral Variations Using Neutron Monitor Time-delay Measurements. *The Astrophysical Journal*, 817, 38.
70. Seo, E., Ahn, H., Beatty, J., Coutu, S., Choi, M., DuVernois, M., et al. (2004). Cosmic-ray energetics and mass (cream) balloon project. *Advances in Space Research*, 33(10), 1777–1785. The Next Generation in Scientific Ballooning.
71. Shea, M., Smart, D., & McCracken, K. (1965). A study of vertical cutoff rigidities using sixth degree simulations of the geomagnetic field. *Journal of Geophysical Research*, 70(17), 4117–4130.
72. Sigl, G. (2012). High energy neutrinos and cosmic rays. *arXiv preprint arXiv:1202.0466*.
73. Skobeltzyn, D. (1929). The Angular Distribution of Compton Recoil Electrons. *Nature*, 123(3098), 411–412.
74. Skobeltzyn, D. V. (1985). The early stage of cosmic ray particle research. In Early History of Cosmic Ray Studies, Springer. pp. 47–52.
75. Stecker, F. W. (1973). Simple Model for Scanning-angle Distribution of Planetary Albedo Gamma-rays. *Nature Physical Science*, 242, 59–60.
76. Stephens, S. A., & Badhwar, G. D. (1981). Production spectrum of gamma rays in interstellar space through neutral pion decay. *Astrophysics and Space Science*, 76, 213–233.
77. Störmer, C. (1934). Critical remarks on a paper by g. lemaître and ms vallarta on cosmic radiation. *Physical Review*, 45(11), 835.
78. Svensson, G. (1958). The cosmic ray photon and π^0-meson energy spectra at 29-30 km above sea-level. *Arkiv Fysik*, 13, 347.

79. Taylor, A. M. (2016). Cosmic rays beyond the knees. *Nature*, 531(7592), 43–44.

80. Thébault, E., Finlay, C. C., Beggan, C. D., Alken, P., Aubert, J., Barrois, O., et al. (2015). International geomagnetic reference field: the 12th generation. *Earth, Planets and Space*, 67(1), 79.

81. Thompson, D. J., Simpson, G. A., & Ozel, M. E. (1981). SAS 2 observations of the earth albedo gamma radiation above 35 MeV. *Journal of Geophysical Research*, 86, 1265–1270.

82. Trenn, T. J. (1976). Rutherford on the alpha-beta-gamma classification of radioactive rays. *Isis*, 67(1), 61–75.

83. Tsyganenko, N. A. (1987). Global quantitative models of the geomagnetic field in the cislunar magnetosphere for different disturbance levels. *Planetary and Space Science*, 35, 1347–1358.

84. Van Allen, J. A., & Frank, L. A. (1959). Radiation around the earth to a radial distance of 107,400 km. *Nature*, 183(4659), 430–434.

85. Van Oosterom, A., & Strackee, J. (1983). The solid angle of a plane triangle. *IEEE Transactions on Biomedical Engineering*, BME-30(2), 125–126.

86. Wallace, J. M., & Hobbs, P. V. (2006). Atmospheric. Science.

87. Watson, A. (2000). Ultra-high-energy cosmic rays: the experimental situation. *Physics Reports*, 333, 309–327.

88. Wilks, S. S. (1938). The large-sample distribution of the likelihood ratio for testing composite hypotheses. *Ann. Math. Statist.*, 9(1), 60–62.

89. Wilson, C. T. R. (1921). Iii. investigations on lighting discharges and on the electric field of thunderstorms. *Philosophical Transactions of the Royal Society of London. Series A, Containing Papers of a Mathematical or Physical Character*, 221(582-593), 73–115.

90. Yoshida, S., Hayashida, N., Honda, K., Honda, M., Imaizumi, S., Inoue, N., et al. (1994). Lateral distribution of charged particles in giant air showers above 1 eev observed by agasa. *Journal of Physics G: Nuclear and Particle Physics*, 20(4), 651.

APPENDICES

APPENDIX A
PARALLEL COMPUTATION OF THE EXPOSURE MAP

A long calculation time from the exposure calculation came from two matrix transformations to accumulate the LAT exposure ~~time~~ when it sees the Earth. ~~Since the FT2 or spacecraft log file is recorded in the position and all metadata.~~

For each step time, the transformation matrix will be calculated from the information of spacecraft orientation. After that, each ~~grid-like~~ nadir angle represented in equatorial coordinate (Equation 4.2.1) was transformed into the plane of detector (Equation 4.6). Hence, we can inspect the incidental from a given nadir angle for summing the LAT exposure time and multiples with the effective area in the visible region.

There is one thing that could be used to approximate the complexity of the code which is the resolution of the exposure map. Assuming that there are M cells in θ_{NADIR} axis and N cells in ϕ_{NADIR} axis. It will cost $\mathcal{O}(MN)$ multiply by the complexity of two transformation matrices to compute a single exposure map. Last but not least, this complexity will be multiplied by 50 times since we have 50 bins that have their own specific mean energy which affects the effective area.

The first version of Python code takes 1434.76 seconds to finish one week of FT2 data. In addition, the matrix transformation is already used Numpy for all matrix operations which means that the plain Python code likely ~~to~~ takes longer than this speed. In the meantime, using serial code with C++ takes around 11.85 seconds to finish the workload of a single week. ~~Meaning that the calculation time is ~120 times faster from the compiling language.~~

The parallel code is implemented in the C++ programming language with Message Passing Interface (MPI). We use Master-Slave techniques for fully

~~utilizing~~ the CPU resources where the master process is monitoring and sending the task to all workers. Consequently, there is only one master process and allows the program to scale horizontally by adjusting the number of slave processes.

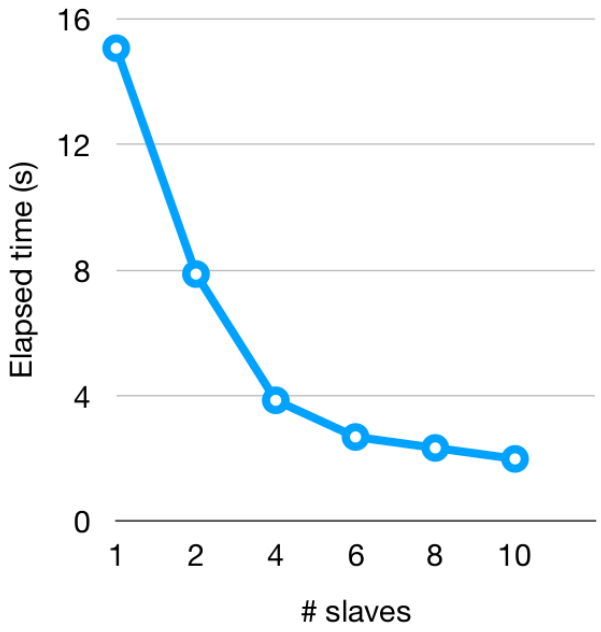

Figure A.1: Benchmarking of the serial and parallel code in the low level language.

The hardware ~~that was~~ used to benchmark compose of 6 cores and 12 threads. Figure A.1 shows the scalability of the code in the exponential trends of the elapsed time and the number of slave processes. The ~~underlying reason why it became a~~ plateau curve on the edge came from the maximum available running threads on this hardware is only twelve which means that the more number of worker that exceeds this limit does not reduce the computation time. However, the total CPU cores on the cluster in space physics laboratory are around 200 thread executors. The performance from running the parallel code in the cluster takes only a dozen hours to finish.

APPENDIX B
POWER LAW IN ENERGY

~~According to~~ Equation 4.7 and Equation 4.8 where the power law is in rigidity. The relation of the power-law spectrum in rigidity could be derived into the energy spectrum as in Equation B.1 and Equation B.2 sequentially.

Single power law (SPL)

The energy spectrum in energy is derived as

$$\frac{dN}{dE} = N_0[E_k(E_k + 2m_p)]^{-\gamma/2}\left(\frac{E_k + m_p}{\sqrt{E_k(E_k + 2m_p)}}\right) \tag{B.1}$$

where m_p is the mass of proton and E_k is the kinetic energy and N_0 is defined as the normalization factor.

Broken power law (BPL)

$$\frac{dN}{dE} = \begin{cases} N_0[E_k(E_k + 2m_p)]^{-\gamma_1/2}\left(\frac{E_k+m_p}{\sqrt{E_k(E_k+2m_p)}}\right) & : \ E < E_{\text{Break}} \\ N_0[E_b(E_b + 2m_p)]^{(\gamma_2-\gamma_1)/2}[E_k(E_k + 2m_p)]^{-\gamma_2/2}\left(\frac{E_k+m_p}{\sqrt{E_k(E_k+2m_p)}}\right) & \\ : \ E \geq E_{\text{Break}} & \end{cases} \tag{B.2}$$

where the symbol is defined in the same way as Equation B.1.

APPENDIX C
SUBTRACTING γ-RAY BACKGROUND

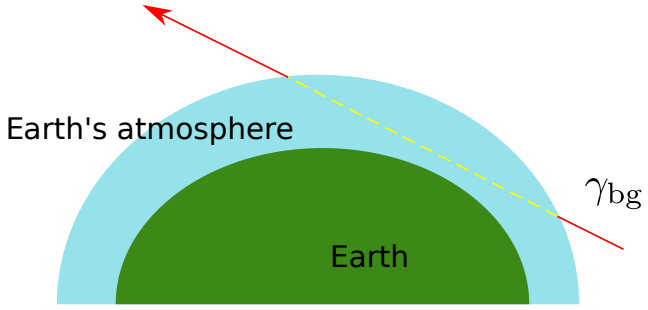

Figure C.1: Schematics of γ-ray propagation from diffusive background

Assuming the probability of the collision process as a classical relation

$$N \equiv N_0 e^{-n\sigma x} \tag{C.1}$$

when

- n is a density of the air
- σ is a crossection of the γ-ray and the air
- x is a propagation length.

From using cross-section data from M.J. Berger (2010), we found that collision probability of γ-ray with a nitrogen atom and oxygen atom very similar in the energy range of our interest. If we consider a worst-case scenario (longest path and highest density that could happen in atmosphere), we found a passing possibility approach to one more than third order. To sum up, we could straightforwardly remove background by taking the average diffusive background per unit of angle before applying.

APPENDIX D
INTERACTION MODEL

Since we know the relation of γ-ray spectrum from incident proton spectrum collide with a nitrogen atom as

$$\frac{dN_\gamma}{dE_\gamma} \propto \int_{E_\gamma}^{E_{\max}} dE' \frac{dN_p}{dE'} \frac{d\sigma^{pN\to\gamma}(E', E_\gamma)}{dE_\gamma}. \tag{D.1}$$

Change to discrete form

$$\frac{dN_\gamma}{dE_\gamma} \propto \sum_{E_\gamma}^{E_{\max}} \frac{E_p}{E_\gamma} \Delta(\ln E') E_\gamma \frac{d\sigma^{pN\to\gamma}}{dE_\gamma} \frac{dN_p}{dE'}, \tag{D.2}$$

and adding first term correction for Helium collision and define $f_{pp} \equiv E_\gamma(d\sigma^{ij\to\gamma}/dE_\gamma)$ ~~which came~~ from K&O model

$$\begin{aligned}\frac{dN_\gamma}{dE_\gamma} &\propto \sum_{E_{\rm CR}=E_\gamma}^{E_{\max}} \frac{E_{\rm CR}}{E_\gamma} \Delta(\ln E_{\rm CR}) \left[E_\gamma \frac{d\sigma^{pN\to\gamma}}{dE_\gamma} \left(\frac{dN_p}{dE_{\rm CR}} \right) + E_\gamma \frac{d\sigma^{HeN\to\gamma}}{dE_\gamma} \left(\frac{dN_{He}}{dE_{\rm CR}} \right) \right] \\ &\propto \sum_{E_{\rm CR}=E_\gamma}^{E_{\max}} \left[\frac{E_{\rm CR}}{E_\gamma} \Delta(\ln E_{\rm CR}) \right] \left[f_{pp} \frac{dN_H}{dE} \left\{ 1 + \frac{\sigma_{\rm HeN}}{\sigma_{\rm pN}} \left(\frac{dN_{\rm H}}{dR} \right)^{-1} \frac{dN_{\rm He}}{dR} \frac{dR_{\rm He}}{dR_H} \right\} \right]\end{aligned} \tag{D.3}$$

In our case, we use the fraction relation of cross-section between different atom number with a limit of relativistic as Atwater & Freier (1986a), we have found $\sigma_{\rm HeN}/\sigma_{\rm pN} \approx 1.77$

Lastly, term $dR_{\rm He}/dR_{\rm H} = 4$ because the relativistic energy mass relation fraction of rigidity between Helium that approximately heavier than proton 4 times.

BIOGRAPHY

NAME	Mr. Patomporn Payoungkhamdee
DATE OF BIRTH	29 April 1996
PLACE OF BIRTH	Bangkok, Thailand
INSTITUTIONS ATTENDED	Mahidol University, 2014–2017
	Bachelor of Science (Physics)
	Mahidol University, 2018–2020
	Master of Science (Physics)
HOME ADDRESS	86/46 Moo. 7, Bangmuang, Muang,
	Samutprakan 10270 Thailand
E-MAIL	patomporn.pay@student.mahidol.ac.th